The within-subject application of diffusion tensor MRI and CLARITY reveals brain structural changes in *Nrxn2* deletion mice

Eleftheria Pervolaraki Ph.D[1]*, Adam L. Tyson MRes[2,3,4]*, Francesca Pibiri Ph.D[5], Steven L. Poulter Ph.D[5], Amy C. Reichelt Ph.D[6], R. John Rodgers Ph.D[7], Steven J. Clapcote Ph.D[1], Colin Lever Ph.D[5], Laura C. Andreae MBBS Ph.D[2,3]*, James Dachtler Ph.D[1,5]*

[1]School of Biomedical Sciences, University of Leeds, LS2 9JT, UK

[2]Centre for Developmental Neurobiology, Institute of Psychiatry, Psychology and Neuroscience, King's College London, London SE1 1UL, UK

[3]MRC Centre for Neurodevelopmental Disorders, King's College London, London SE1 1UL, UK

[4]Department of Forensic and Neurodevelopmental Sciences, Institute of Psychiatry, Psychology and Neuroscience, King's College London, London SE5 8AF, UK

[5]Department of Psychology, Durham University, South Road, Durham, DH1 3LE, UK

[6]Robarts Research Institute, Western University, London, Ontario, Canada, N6A 5B7, Canada

[7]School of Psychology, University of Leeds, LS2 9JT, UK

*These authors contributed equally.

Address for Correspondence: Dr J Dachtler, Department of Psychology, Durham University, South Road, Durham, DH1 3LE, UK. Email: james.dachtler@durham.ac.uk

Abstract

Background

Of the many genetic mutations known to increase the risk of autism spectrum disorder, a large proportion cluster upon synaptic proteins. One such family of presynaptic proteins are the neurexins (NRXN), and recent genetic and mouse evidence has suggested a causative role for *NRXN2* in generating altered social behaviours. Autism has been conceptualised as a disorder of atypical connectivity, yet how single-gene mutations affect such connectivity remains under-explored. To attempt to address this, we have developed a quantitative analysis of microstructure and structural connectivity leveraging diffusion tensor MRI (DTI) with high-resolution 3D imaging in optically cleared (CLARITY) brain tissue in the same mouse, applied here to the *Nrxn2α* knockout (KO) model.

Methods

Fixed brains of *Nrxn2α* KO mice underwent DTI using 9.4T MRI, and diffusion properties of socially-relevant brain regions were quantified. The same tissue was then subjected to CLARITY to immunolabel axons and cell bodies, which were also quantified.

Results DTI revealed decreases in fractional anisotropy and increases in apparent diffusion coefficient in the amygdala (including the basolateral nuclei), the anterior cingulate cortex, the orbitofrontal cortex and the hippocampus. Radial diffusivity of the anterior cingulate cortex and orbitofrontal cortex was significantly increased in *Nrxn2α* KO mice, as were tracts between the amygdala and the orbitofrontal cortex. Using CLARITY, we

find significantly altered axonal orientation in the amygdala, orbitofrontal cortex and the anterior cingulate cortex, which was unrelated to cell density.

Conclusions

Our findings demonstrate that deleting a single neurexin gene (*Nrxn2α*) induces atypical structural connectivity within socially-relevant brain regions. More generally, our combined within-subject DTI and CLARITY approach presents a new, more sensitive method of revealing hitherto undetectable differences in the autistic brain.

Key Words

MRI, CLARITY, social, autism, axons, diffusion, structure, imaging

Background

Autism is a common neurodevelopmental disorder, which is highly heritable (1). While heritability is high, it is also clear that autism is highly polygenic. Around ~400-1000 genes are involved in autism susceptibility (2-5). Many of these genes cluster upon proteins relating to synaptic signaling (6). A family of presynaptic proteins garnering recent interest have been the neurexins (*NRXNs*). NRXNs are encoded by three genes (*NRXN1, NRXN2, NRXN3;* note that *CNTNAP1* and *CNTNAP2* are sometimes referred to as *NRXN4*), of which two major isoforms exist: the longer α proteins with six laminin/neurexin/sex hormone (LNS) binding domains, and the shorter β proteins with one LNS binding domain (7, 8).

78 Mutations within all three *NRXN* genes have been linked to autism (6).
79 Heterozygous deletions within *NRXN2* have been identified in a number of
80 individuals with autistic phenotypes. These include an autistic boy and his
81 father (who had severe language delay but not autism) who both had a
82 frameshift mutation within exon 12 of *NRXN2* (9); a 570-kb de novo deletion
83 of 24 genes at chromosome 11q13.1, including *NRXN2*, in a 21-year old man
84 displaying a clinical phenotype including autistic traits (10); a 1.6Mb deletion
85 at chromosome region 11q12.3-11q13.1, including *NRXN2*, in a 23-year old
86 man with intellectual disability and behavioral problems (11); a de novo
87 frameshift mutation identified in a Chinese man with autism spectrum disorder
88 (ASD) (12), a 921 kb microdeletion at 11q13 in a 2 year old boy who had
89 language and developmental delay (although did not meet the autism
90 diagnosis criteria) (13) and a paternally inherited microRNA miR-873-5p
91 variant in an ASD individual which altered binding affinity for several risk-
92 genes including *NRXN2* and *CNTNAP2* (*NRXN4*) (14). Furthermore, recently,
93 two large-scale reports have identified *NRXN2* with ASD risk. A study of 529
94 ASD patients and 1,923 controls in a Chinese population identified two
95 *NRXN2* variants which significantly increase ASD risk (15). The second study
96 employed machine learning approaches across 5000 ASD families to rank the
97 importance of ASD candidate genes, and ranks *NRXN2* in the top ~0.5% of
98 genes, i.e. 113th (16). For comparison, *NRXN1*, for which the evidence base
99 for its links to ASD is broader and stronger, ranks 45, and *CNTNAP2* ranks
100 211th (16). Consistent with these association studies, we and others have
101 previously found that homozygous or heterozygous deletion of *Nrxn2*α
102 induces impairment in social approach and social recognition (17-19). In

103 summary, although mutations within *NRXN2* are rare, understanding how they
104 may drive social, ASD-relevant behavioural changes is important. One
105 important goal is to help elucidate how apparently convergent
106 pathophysiology in ASD emerges despite marked genetic heterogeneity
107 (Insert ref Geschwind & State, 2015 cited above); mapping brain alterations
108 driven by different single genes is thus a crucial task.
109
110 Currently it is unknown whether deletion of *Nrxn2*α changes the brain's
111 microstructure and connectivity. One previous study found coarse alterations
112 to cell layer thickness within the hippocampus of *Nrxn2*α homozygous KOs
113 (20). However, cell density measurements are unlikely to reveal the true
114 extent of changes within the autistic brain. Within the current study, we have
115 addressed this by developing a dual imaging approach (DTI and CLARITY)
116 that quantifies the alignment and density of white matter, applied here to brain
117 regions known to support social behavior in a mouse model of autism.
118
119 Diffusion tensor MRI (or DTI) is based upon the movement of water
120 molecules, a measure that is termed fractional anisotropy (FA). Apparent
121 diffusion coefficient (ADC) is similar to FA, but quantifies diffusion restriction
122 as opposed to the spatial symmetry of diffusion. This approach has been used
123 to explore neuropathological markers in autistic patients; alterations in
124 myelination, axonal abundance, size and orientation all modify FA and ADC
125 values (21-23). Using the preferred direction of the diffusion of tensors
126 between brain regions can be used to explore their potential connection.
127 Quantification of those computed streamlines by FA and axial and/or radial

diffusion can indicate impairments in regional structural connectivity. Since aberrant brain connectivity is likely a core feature of autism (24), we reasoned that the candidate method for probing the autistic brain should combine tractographic techniques. Accordingly, here, we combined high resolution imaging of labelled neuronal tracts in brains rendered transparent by CLARITY with DTI.

CLARITY is a recent development that renders tissue optically transparent and macromolecule permeable (25). This permits antibody staining and imaging of much larger tissue volumes than possible under traditional immunofluorescence techniques. By examining fiber orientation without sectioning-related artefacts and biases, axonal staining in cleared tissue affords a deeper understanding of the microstructure and structural connectivity of a brain region.

Given the social impairments found within *Nrxn2α* mice, we sought to examine those brain regions most closely linked with social behavior (See Supplemental Materials). Briefly, we identified four regions of interest (ROIs): the amygdala, and three brain regions strongly and directly connected to the amygdala; the hippocampus, orbitofrontal cortex (OFC), and anterior cingulate cortex (ACC). As predicted, structural connectivity was abnormal in *Nrxn2α* mice.

Methods

Ethics

153 All procedures were approved by the University of Leeds and Durham
154 University Animal Ethical and Welfare Review Boards and were performed
155 under UK Home Office Project and Personal Licenses in accordance with the
156 Animals (Scientific Procedures) Act 1986.
157
158 **Animals**
159 Full details of the animals, their background, genotyping and housing can be
160 found elsewhere (17). In brief, male B6;129-
161 *Nrxn3tm1Sud*/*Nrxn1tm1Sud*/*Nrxn2tm1Sud*/J mice (JAX #006377) were
162 purchased from the Jackson Laboratory and outbred once to the
163 C57BL/6NCrl strain (Charles River, Margate, United Kingdom) to obtain mice
164 that were individually Nrxn2α KO heterozygotes. Subsequently, HET knockout
165 males were bred with HET females (cousin mating).
166
167 **Experimental animals**
168 6 adult wild-type males (Charles River, Margate, UK) and 6 age matched
169 littermate Nrxn2α KO homozygotes (71 days ± 6 days old (SEM)) were
170 perfused-fixed with 4% paraformaldehyde (PFA) in 0.1 M phosphate buffer
171 saline (PBS) and the brains extracted. The brains were immersed in 4%
172 PFA/0.1 M PBS for a minimum of 48 hours prior to imaging. During imaging,
173 the samples were placed in custom-built MR-compatible tubes containing
174 Fomblin Y (Sigma, Poole, Dorset, UK).
175
176 Due to the relatively low variance, and owing to the complexity and
177 methodological nature in our experimental approach, we achieved

178 significance by groups of 6 (power provided in Results). No data was
179 excluded from the study. Sample randomisation was performed by JD, with
180 experimenters (EP and ALT) blinded to genotype.
181
182 **Data Acquisition**
183 Image acquisition has been described elsewhere (26). Each brain was 3D
184 imaged using the protocol TE: 35 ms, TR: 700 ms and 10 signal averages.
185 The field of view was set at 128 x 128 x 128, with a cubic resolution of 100
186 μm/pixel and a b value of 1200 s/mm^2. Further details can be found in
187 Supplemental Materials.
188
189
190 **Image Processing**
191 Parsing of the raw data was semi-automated using DSI Studio, in order to
192 obtain b-values for every normalized gradient vector on the x, y and z
193 orientations. Unwanted background, setting a threshold, smoothing of the
194 data and definition of tissue boundaries was performed prior to the
195 reconstruction of the final 3D image. DTI analysis parameters were calculated
196 as previously described (28).
197
198 The *ex vivo* mouse brain 3D diffusion-weighted images were reconstructed
199 from the Bruker binary file using DSI Studio (http://dsi-studio.labsolver.org)
200 (29). Direction Encoded Colour Map (DEC) images were generated by
201 combining the information from the primary eigenvectors, diffusion images
202 and the FA. Images of the primary vectors and their orientation were

203 reconstructed and superimposed on corresponding FA images to guide the
204 segmentation of discrete anatomical locations according to the brain atlas
205 (Figure 1B-D). Region of interest definition was performed by author EP and
206 corroborated independently by JD, with region area compared between the
207 experimenters (data not shown). We identified a canonical coronal slice (100
208 μm) for a given ROI from the standard mouse brain atlas (Figure 1A-D; Supp.
209 Figure 1) (27). We analysed three coronal slices centred on the canonical
210 slice, totalling 300 μm in anterior/posterior extent. For whole brain region
211 analysis, we used a similar approach, except regions were segmented for
212 every other slice in the anterior to posterior extent. The DSI Studio DTI
213 reconstruction characterizes the major diffusion direction of the fibre within the
214 brain (30, 31). Extraction of FA (calculated (26)) and ADC was performed
215 within selected segmented brain areas for every 3D reconstructed mouse
216 brain.
217

218 **Regions of Interest (ROIs)**

219 Our DTI approach was to undertake an *a posteriori* analysis of neural
220 organization in regions of interest (ROIs) identified by previous literature as
221 socially-relevant. Given the social impairments found within *Nrxn2*α mice, for
222 the current study, we identified the brain regions of interest (ROIs) most
223 closely linked with social behavior, using previously published reports of brain
224 region involvement in social behaviour. Quantification of c-Fos
225 immunoreactivity has highlighted the importance of several amygdala nuclei
226 (including the basolateral) following social exposure (32), but also the anterior
227 cingulate cortex (ACC), prefrontal cortex and the hippocampus (33). Lesions

228 to the primate amygdala alter social interactions (34, 35), and amygdala
229 neurons in primates including humans increase firing rates during social
230 scenarios (36-38). Consistent with these animal studies, amygdala damage in
231 humans (39) and amygdala dysfunction in ASD patients (40) impair social
232 responses. Other socially-important brain regions have also been proposed.
233 Notably, several studies have implicated the rodent hippocampus in social
234 behavior, including social memory and sociability (41-43). For instance,
235 intrahippocampal administration of neurolide-2, which interacts with α-
236 neurexin, specifically impairs sociability, but not anxiety and spatial learning in
237 rats (44). These findings are consistent with reports of social deficits in
238 humans with hippocampal damage (45) and hippocampal abnormalities in
239 ASD (46, 47). Finally, several studies link the frontal cortex, particularly the
240 orbitofrontal cortex, which is strongly anatomically connected with the
241 amygdala(48), to social processing (49, 50), consistent with findings of
242 abnormalities in orbitofrontal cortex in ASD (48, 51). Control regions of the
243 primary motor cortex (M1), primary sensory cortex (S1) and the barrel field
244 were chosen for CLARITY (Supp. Figure 12N-O).
245

246 **CLARITY**

247 Following MR imaging, the brains were washed in PBS to remove all Fomblin
248 Y and then incubated for 7 days in hydrogel solution at 4°C prior to
249 polymerisation at 37°C for 3.5 hours. The tissue was cut into 1.5 mm coronal
250 sections using a custom 3D-printed brain-slicing matrix based on MRI scans
251 of an adult C57BL/6 mouse brain (52) and incubated in clearing buffer for 24
252 days at 37°C with shaking. The cleared tissue was then washed in $PBSTN_3$

253 (0.1% TritonX-100 and 1.5 mM sodium azide in PBS) for 24 hours at room
254 temperature and incubated in primary antibody solution (neurofilament (Aves
255 NF-H) 1:100 in $PBSTN_3$) at 37°C with shaking for 13 days. Samples were
256 washed, and then incubated in secondary antibody (AlexaFluor 488 goat anti-
257 chicken IgY) as per the primary. Sections were washed again, and incubated
258 in 3.6 μM DAPI (4',6-diamidino-2-phenylindole) followed by 85% glycerol in
259 PBS for refractive index matching.
260
261 Cleared samples were imaged using a Zeiss 7MP multiphoton microscope at
262 770 nm using a 20x objective lens (W Plan-Apochromat, NA 1.0, WD 1.7
263 mm). Images (512 x 512 x 512 voxels or 265 x 265 x 265 μm with an isotropic
264 resolution of 520 nm) were acquired in ACC, basolateral (BLA) and
265 basomedial amygdala and OFC) in both hemispheres. DAPI and
266 neurofilament signal was segmented into cell nuclei and axons, and the
267 resulting binary images were used to generate values for cell density, axonal
268 density and axonal alignment.
269
270 Full CLARITY methodological details are available within Supplemental
271 Materials.
272
273 **Data Availability**
274 Codes to analyse CLARITY datasets are made available by author LCA by
275 email request to either JD or LCA, subject to reference to the current paper.
276 The datasets used and/or analysed during the current study are available
277 from the corresponding author on reasonable request.

278

279 **Data Analysis**

280 All data are expressed as mean ± standard error of the mean (SEM). To
281 assess the variance between genotypes within a single brain structure across
282 hemispheres (given the importance of hemispheric differences in ASD (53)),
283 data was analyzed by within subject repeated measures two-way ANOVAs,
284 with Sidak multiple corrections employed on post hoc testing, or unpaired T-
285 tests. To correct for multiple comparisons, we employed the Benjamini-
286 Hochberg Procedure (corrected P values stated). Non-significant statistical
287 results, particularly hemisphere comparisons, can be found in Supplemental
288 Materials. Statistical testing and graphs were made using GraphPad Prism
289 version 6 and SPSS v22.

290

291 **Results**

292 ***Nrxn2α* deletion disrupts DTI measures of microstructure in social brain**
293 **regions**

294 To assess whether *Nrxn2α* deletion alters gross morphology, we quantified
295 whole brain volume using DTI. We found total brain volume for wild-types and
296 *Nrxn2*α KOs was similar (456.0 ± 14.76 vs. 466.2 ± 11.0 mm^3 (respectively);
297 $t_{(10)} = 0.55$, $p = 0.59$). Thus, Nrxn2α deletion does not change total brain size.

298

299 To quantitatively measure DTI, we examined FA and ADC. FA analyses
300 changes in the linear orientation (i.e. along an axonal tract), whereas ADC
301 (mean diffusivity) averages diffusion in all directions (i.e. the X, Y and Z axis),
302 which is sensitive to changes such as altered alignment. The amygdala is

303 critically important for social behaviours. To assess whether amygdalar
304 alterations might account for social impairments in Nrxn2α KO mice, we
305 segmented the whole amygdala structure and the basolateral nuclei along the
306 anterior-posterior axis.
307
308 The posterior amygdala showed a significant reduction in FA in *Nrxn2α* KO
309 mice (Figure 2A-B) (anterior: genotype ($F_{(1, 10)} = 5.81$, $p = 0.056$); posterior:
310 genotype ($F_{(1, 10)} = 11.2$, $p = 0.025$, power = 85.4%)). This FA reduction was
311 also observed specifically in the BLA, a region strongly associated with social
312 behaviours (Figure 2C; genotype ($F_{(1, 10)} = 6.31$, $p = 0.049$, power = 62.1%)).
313 ADC was not significantly altered in the anterior amygdala, posterior
314 amygdala or BLA (Figure 2D-F; all genotype: $F_{(1, 10)} < 1$).
315
316 We conducted the same analysis for the two prefrontal regions implicated in
317 social behaviour and autism: the OFC and ACC. The pattern of results was
318 similar for both regions: FA was not altered, while ADC was increased in the
319 OFC (Figure 3A-B) and the ACC (Figure 3C-D). FA for the OFC was not
320 significantly altered (genotype: ($F_{(1, 10)} = 3.04$, $p = 0.079$)) but ADC was
321 significantly increased (genotype: ($F_{(1, 10)} = 8.20$, $p = 0.043$, power = 73.3%)).
322 The ACC was unaltered in FA ($t_{(10)} = 1.70$, $p = 0.08$) but had significantly
323 increased ADC ($t_{(10)} = 7.52$, $p = 0.002$, power = 99.9%).
324
325 We sought to examine whether changes in the amygdala (Supp. Figure 4),
326 OFC or ACC FA and ADC were driven by diffusion in the primary axis (λ_1) or
327 the radial orientations (λ_2 and λ_3) by characterisation of AD (primary) and RD

328 (radial). Within the OFC (Figure 3E-F), AD was significantly increased
329 (genotype: ($F_{(1, 10)}$ = 10.74, p = 0.029, power = 83.9%)), as was RD (genotype:
330 ($F_{(1, 10)}$ = 18.26, p = 0.009, power = 97.0%)), suggesting that both along-tract
331 diffusion and tract branching were affected. However, in the ACC (Figure 3G-
332 H), only RD was significantly increased ($t_{(10)}$ = 5.65, p = 0.007, power =
333 99.9%), with no alteration in AD ($t_{(10)}$ = 1.69, p = 0.09). Increased RD is
334 thought to reflect demyelination or changes in axonal density or orientation
335 (54).
336

337 **DTI reveals altered hippocampal microstructure in *Nrxn2α* KO mice**

338 The hippocampus has recently been associated with social motivation and
339 social recognition. Since the specific contributions of the dorsal and ventral
340 hippocampal poles remain unclear, we segmented the whole hippocampus
341 into anterior (Bregma -1.94 mm), middle (Bregma -2.46 mm) (both dorsal) and
342 posterior (Bregma -3.28 mm) (incorporating ventral regions) levels.
343

344 FA values in the anterior, mid and posterior hippocampus were not
345 significantly altered (see Supp. Table 1 for statistics and Supp. Figure 5A-C).
346 Similarly, ADC was unaltered for the anterior and mid hippocampus (Supp.
347 Table 1 for statistics and Supp. Figure 5D-E), but was significantly increased
348 in *Nrxn2α* KO mice in the posterior hippocampus (genotype: ($F_{(1, 10)}$ = 8.80, p
349 = 0.036, power = 76.6%); Supp. Figure 5F). There were no significant
350 genotype differences in AD in any of the hippocampal regions (Supp. Figure
351 6A-C). However, RD was significantly increased in the posterior hippocampus
352 in *Nrxn2α* KO mice (genotype: ($F_{(1, 10)}$ = 10.83, p = 0.027, power = 84.2%;

353 Supp. Figure 6F) but not in anterior and mid regions (see Supp. Table 1;
354 Supp. Figure 6D-E). The theoretical approach undertaken hitherto was to
355 segment ROIs using a single coronal plane (as outlined in the Methods),
356 which subsequently allowed for the same anterior/posterior region to be
357 analysed by CLARITY. However, this restricted analysis could theoretically
358 miss diffusion differences across a whole brain region (as in, for example, the
359 entire anterior to posterior ACC). As a further quantification, we segmented
360 whole regions for the amygdala (Supp. Figure 7), the anterior and posterior
361 hippocampus (Supp. Figure 8) and the OFC and ACC (Supp. Figure 9). We
362 found that although there were more statistical differences between the
363 genotypes for the 'whole' anterior hippocampus region compared to the
364 'single plane' analysis, overall the two analysis methods suggested broadly
365 similar structural alterations.
366
367 Lastly, given DTI is most commonly associated with analysis of white matter
368 tracts, we also quantified the corpus callosum. Changes within the corpus
369 callosum have repeatedly been highlighted in autism (55, 56), including
370 mouse models of autism (57, 58). Here, we found significantly increased FA
371 and reduced ADC in *Nrxn2*α KO mice, which were driven by a significant
372 reduction in RD (Supp. Figure 10).
373
374 In summary, the microstructural measures most altered by *Nrxn2*α deletion
375 were increases in ADC and RD, including in the hippocampus, in line with
376 recent work suggesting a role for ventral hippocampus in social memory (43).
377

DTI tractography reveals *Nrxn2α* deletion affects strucutral connectivity between the amygdala and orbitofrontal cortex

The amygdala is strongly and bidirectionally connected to both the hippocampus (59) and the OFC (60). As all three regions are themselves important for social behaviour, and autism is thought to be, at least in part, related to abnormal structural connectivity (24), we performed tractography analysis between the amygdala (and specifically the BLA) and the hippocampus, and between the amygdala and the OFC.

From the anterior amygdala, we examined the diffusivity (AD and RD) of connections to the anterior and posterior hippocampus (Supp. Figure 11). We did not observe differences in RD in the tracts connecting the amygdala with the hippocampus (see Supp. Table 2 for non-significant statistics). Although AD between the anterior amygdala and anterior hippocampus did not differ by genotype, there was a significant interaction between genotype and hemisphere (genotype x hemisphere ($F_{(1, 10)}$ = 12.12, p = 0.023, power = 88.0%; Figure 4A); post hoc analysis shows this was driven by larger right-vs-left hemisphere AD values within the *Nrxn2α* KOs only (p = 0.012). This difference could be driven by the BLA; there was increased AD in both the BLA/anterior hippocampus tracts (genotype x hemisphere ($F_{(1, 10)}$ = 10.53, p = 0.032, power = 83.2%) and the BLA/posterior hippocampus tracts (genotype x hemisphere ($F_{(1, 10)}$ = 12.97, p = 0.020, power = 90%), which again was related to larger right-vs-left hemisphere values in the *Nrxn2α* KOs (BLA/anterior hippocampus: p = 0.004 and BLA/posterior hippocampus: p = 0.001, (Figure 4C-D)) but not the wild-type (anterior: p = 0.87; posterior: p =

403 1.00). These results indicate that there are differences for the structural
404 connectivity of the amygdala with the hippocampus within the left and right
405 hemisphere in *Nrxn2α* KO mice, with increased axial diffusivity in the right
406 hemisphere. This finding is particularly interesting, as hemispheric differences
407 in functional connectivity, particularly affecting connections from the right
408 amygdala, have been found children with ASD (61, 62).
409
410 Finally, we tested connections between the amygdala and the OFC. For AD,
411 wild-type and Nrxn2α KO mice did not differ by genotype (Figure 4E:
412 genotype: ($F_{(1, 10)} = 2.85$, $p = 0.09$), hemisphere: ($F_{(1, 10)} = 6.38$, $p = 0.052$). RD
413 was strikingly higher in *Nrxn2α* KO mice (Figure 4F: genotype: ($F_{(1, 10)} = 26.06$,
414 $p = 0.023$, power = 99.5%)), indicative of a change in demyelination, axonal
415 density or orientation (54).
416
417 **CLARITY reveals fibre disruption in *Nrxn2α* KO mice in the amygdala,**
418 **orbitofrontal cortex, and anterior cingulate cortex**
419 To further explore the differences as revealed by DTI, we performed CLARITY
420 on the same brain tissue used in DTI, and stained with neurofilament and
421 DAPI to label axons and cell bodies, respectively. We were then able to derive
422 both the axonal alignment (as in, the geometric alignment of axons (from
423 linear alignment to random) within 3D space (see Supp. Figure 2)) and
424 density of the stained fibers, in addition to the cell density.
425
426 The pattern of results was broadly similar for both the prefrontal cortical ROIs.
427 That is, first, axonal alignment was increased in *Nrxn2α* KO mice in the ACC

428 (Figure 5D: genotype: ($F_{(1, 10)}$ = 16.06, p = 0.011, power = 94.9%) but not the
429 OFC (Figure 5G: genotype: ($F_{(1, 10)}$ = 5.56, p = 0.059). Second, this could not
430 be explained by a difference in cell density, since that was similar between the
431 KO and wild-type mice in both the ACC (Figure 5F: genotype: ($F_{(1, 10)}$ <1),
432 hemisphere: ($F_{(1, 10)}$ = 1.73, p = 0.11) and the OFC (Figure 5H: genotype: ($F_{(1,}$
433 $_{10)}$ = 3.09, p = 0.08). An increase in axonal density in *Nrxn2α* KO mice was
434 reliable in the ACC (Figure 5E: genotype: ($F_{(1, 10)}$ = 14.64, p = 0.014, power =
435 93.0%), but not in the OFC (Figure 5H: genotype: ($F_{(1, 10)}$ = 3.09, p = 0.083).
436
437 We further examined two regions of the anterior amygdala, the BLA and
438 basomedial (BMA) nuclei, where altered social cellular responses have been
439 reported in human autism (38). We did not observe any significant differences
440 for axonal alignment or fibre density in the BLA (see Supp. Figure 12A-C), but
441 whereas axonal alignment (Figure 5J, genotype: $F_{(1, 10)}$ = 7.70, p = 0.045,
442 power = 70.6%) but not axonal density (Figure 5K: genotype: ($F_{(1, 10)}$ = 6.10, p
443 = 0.054) was increased in *Nrxn2α* KO mice in the basomedial nuclei, while
444 cell density was unaffected (Figure 5L: genotype: ($F_{(1, 10)}$ <1). Alterations in
445 axonal alignment and density as directly revealed by CLARITY could explain
446 the increases in diffusivity and RD in the prefrontal regions, as measured by
447 DTI.
448
449 To test the specificity of these alterations, we examined three further brain
450 regions; the primary motor cortex (M1; Supp. Figure 12D-F), the primary
451 somatosensory cortex (S1; Supp. Figure 12H-J) and the barrel field (BF;
452 Supp. Figure 12K-M). Interestingly, although there were differences between

453 the hemispheres, there were no statistical differences between the genotypes
454 or genotype x hemisphere interactions for any measure (Supp. Table 3),
455 suggesting some specificity of the alterations in social-relevant brain regions
456 in *Nrxn2α* KO mice.
457
458 In summary, in both the prefrontal ROIs, namely the OFC, and the ACC, DTI
459 showed that ADC and RD were increased in *Nrxn2α* KO mice, likely related to
460 complementary analysis from CLARITY showing that axonal alignment was
461 altered in *Nrxn2α* KO mice in both prefrontal ROIs.
462
463 **Discussion**
464 Interestingly, the single-gene deletion of *Nrxn2α* captures several key aspects
465 of human ASD. In terms of behaviour, three studies have now found social
466 deficits associated with *Nrxn2α* KO (17-19); in terms of brain structure, as
467 reported here (summarised below), the *Nrxn2α* KO mouse model shows
468 altered microstructure and structural connectivity patterns in socially-relevant
469 brain regions reminiscent of changes in ASD.
470
471 A DTI approach has been used for some time to explore neuropathological
472 markers in autistic patients; alterations in myelination, axonal abundance, size
473 and orientation all modify FA and ADC values (21, 63), specifically by
474 reducing amygdala FA (23, 63), and have been used as a quantitative
475 measure of changes to brain white matter integrity (23, 24). Increased cortical
476 ADC typically indexes reduced functionality: e.g. increased hippocampal ADC
477 is associated with mild cognitive impairment (64, 65) and predicts verbal and

visuospatial memory in old healthy controls (66). Furthermore, both increased RD of various white matter tracts (67, 68) and increased whole-brain AD (68) have been observed in ASD. The *Nrxn2α* KO mouse reproduces many of these specific changes, including reduced FA and increases in ADC, AD and RD. Whole brain increases in ADC, AD and RD (but not FA) have been reported in ASD children, as have increases in ADC and RD in frontal cortex tracts (68). This is in agreement with other studies noting increased ADC in frontal cortex in ASD (63), as we observed here in both the prefrontal regions examined, the OFC and ACC. Likewise, FA was reduced in the amygdala in ASD children and adolescents (69), and right-sided lateralisation of abnormal amygdala/hippocampus-related connections, as seen in our *Nrxn2α* KO mouse, has been noted in high-functioning adolescents/adults with autism (70).

Whilst the current study specifically explores structural connectivity, it is difficult to extrapolate as to what these structural changes mean for functional connectivity in the *Nrxn2α* KO mouse. Hyper and hypo connectivity theories of autism have remained contentious, and vary in humans by cohort studied (e.g. by age of participant) (71). Further, in studies that have combined resting state functional MRI (rsfMRI) and DTI, functional and structural connectivity do not always overlap (72-74). Our current data suggests that DTI differences can be explained by altered axonal patterning (i.e. CLARITY). Others have explored the biological mechanisms linking structural connectivity to altered functional connectivity. Zhan et al. (2014) found that deletion of the chemokine receptor Cx3cr1 resulted in impaired synaptic pruning of long-

503 range connections during development, which manifested as impaired social
504 behavior caused by decreased frontal functional connectivity, reduced
505 synaptic multiplicity and weakened coherence of local field potentials (75).
506 Thus, it is possible that impairments in neuronal structural maturation can
507 generate functional connectivity deficits that encapsulate core autism
508 phenotypes.
509
510 Our findings corroborate these quantifications of clinical autism, but highlights
511 the question of what do the different measures of ADC, FA, AD and RD
512 represent? Importantly, we observed these microstructural changes in various
513 socially-relevant brain regions against a background of unchanged cell
514 density in all our study's ROIs. Unexpectedly, this highlights the power of our
515 new approach. Dudanova et al. (2007) concluded from measures of cell
516 counting and cortical cell layer thickness that NRXN2 played little role in
517 normal brain development (20). Indeed, in earlier studies, it was suggested
518 that deletion of all *Nrxns* was unlikely to affect synaptic development but
519 instead disrupts synaptic function (76). We propose that measures such as
520 two-dimensional cell counting may be underestimating the impact of genetic
521 mutations upon normal development. By staining cleared brain tissue with a
522 nuclear marker and performing automated three-dimensional cell counting, we
523 found no effect of *Nrxn2α* deletion on cell density in any region of interest
524 examined. But this belies the clear effects upon microstructure integrity across
525 multiple regions as measured by both DTI and CLARITY, and its specificity;
526 only the socially-relevant brain regions we tested were disrupted, and not
527 primary sensory or motor regions. Future studies will benefit from employing

528 more sensitive measures of brain structural connectivity to determine the
529 relevance of genetic mutations in development.
530
531 FA and ADC can be influenced by changes in axonal density and alignment
532 (e.g. by myelination, demyelination, axonal damage, loss of white matter
533 coherence (77)). It is likely that the axonal alignment metric used to quantify
534 CLARITY more closely reflects the ADC measure of DTI, given that ADC (or
535 mean diffusivity) equally weights diffusion across all eigenvectors and does
536 not bias the primary eigenvector as FA does. Thus, it is likely that alterations
537 in the properties of axons in *Nrxn2α* KO mice are driving these changes in FA
538 and ADC. Given we mostly see differences in RD, thought to reflect tract
539 branching and myelination (as it measures λ_2 and λ_3), it is possible that the
540 orientation in the perpendicular not parallel orientation of fibres is mostly
541 affected. Given the differences in the amygdala, OFC and ACC, it is possible
542 that even though neuronal densities are similar in the *Nrxn2α* KO brain, it is
543 the connections between neurones and brain regions that are perturbed. This
544 would be consistent with the idea that structural connectivity disruption may
545 represent a core feature of autism (78). A broader question is how does the
546 loss of *Nrxn2α* account for changes in axonal organisation? Ultimately, this
547 question requires further studies. Others have shown that in *Nrxn2α* KO mice,
548 excitatory transmitter release is reduced, as is short-term plasticity (18).
549 Reduced glutamatergic release, even at a relatively long range to the
550 synapse, can change the complexity of dendritic arbors (79). As this is a gene
551 deletion model, it is conceivable that altered glutamatergic signalling during
552 early development impairs appropriate synapse maturation, leading to the

553 structural changes we see herein. Further, how or whether these structural
554 changes fully explain the social impairments of *Nrxn2α* KO mice would require
555 new studies. Conceivably, inducible knock-down of *Nrxn2* (by inducible
556 knockout, siRNA, optogenetics etc.) within a specific brain region would
557 provide evidence that social abnormalities are being driven by *Nrxn2* loss.
558 However, developmentally-dependent altered structural connectivity would be
559 harder to definitively manipulate to explain changes in social behaviours.
560
561 Here we have developed a new application of CLARITY to quantitatively
562 investigate disease models by combining DTI with high resolution 3D imaging
563 and automated analysis of axonal fibres in a within subject study. Inevitably,
564 there are some technical limitations that will require future refinement as this
565 technology matures.
566
567 First, while we used CLARITY and immunolabeling to identify axons, we
568 cannot know whether axon-related changes alone reflect all the changes we
569 observed for our DTI measures. Second, whilst we can segment entire brain
570 regions for DTI analysis, it was not practical to image larger brain areas at the
571 necessary resolution for CLARITY. While it is theoretically possible that we
572 may bias sampling of each brain region by picking ROIs for multiphoton
573 imaging, this was done using atlas-defined coordinates and by an
574 experimenter blind to the DTI results, so minimising any bias. However, within
575 the current study, we were only able to apply the CLARITY approach to the
576 amygdala, OFC and ACC. It was not practical to apply this methodology to the
577 hippocampus, due to its extremely heterogeneous structure. The small cubic

578 ROIs could not be reproducibly positioned, and larger ROIs to average across
579 larger areas of the hippocampus were not possible. Although imaging of fibre
580 tracts in large volumes of cleared tissue is possible (80), fluorescent labelling
581 limitations make it impractical for a study of this nature. Despite this, as the
582 adoption of the CLARITY technique increases, we hope that the use of DTI
583 and CLARITY to study structural connectivity across spatial scales will
584 become commonplace.
585
586 As yet, no one DTI protocol has emerged as the standard for *in vivo* or *ex vivo*
587 imaging. Indeed, there has been debate regarding the best number of
588 diffusion gradients to use, among other parameters (81). Whilst some claim a
589 minimum of 30 directions are required to estimate anisotropy (81), others
590 claim that the benefits of using more than six are limited (82-85). A limitation
591 of these studies is that these competing claims have not been complemented
592 with standard neuroanatomical techniques. Where we found DTI differences,
593 these were corroborated by the quantification of CLARITY (OFC, ACC, with
594 BLA differences not reaching statistical significance after multiple-comparison
595 correction). A further potential limitation of the current study is that groups of
596 six animals may be underpowered. We argue for our approach here as
597 follows. First, low variance in the datasets permits smaller group sizes.
598 Second, for 18 of our 22 significant results, the observed power was more
599 than 80%. Third, given the technical complexity of this approach, particularly
600 in its early adoption and refinement stages, large sample throughput of
601 multiple brain regions is challenging.
602

In summary, our combined use of DTI and CLARITY has revealed changes in microstructure and structural connectivity of socially-relevant brain regions in *Nrxn2α* KO mice that may underlie their deficits in social behaviour. It is hard to conceive how these changes could have been observed using classical experimental approaches. We envisage this approach will deliver a new level of detail in structural connectivity approaches to understanding autism.

Abbreviations

ACC: anterior cingulate cortex

AD: axial diffusivity

ADC: apparent diffusion coefficient

ASD: autism spectrum disorder

BLA: basolateral amygdala

CLARITY: optically cleared brain tissue

DTI: diffusion tensor imaging

FA: fractional anisotropy

OFC: orbitofrontal cortex

Nrxn2: neurexin II

RD: radial diffusivity

ROI: region of interest

Declarations

Ethics approval and consent to participate

All experiments were performed under UK Home Office Project and Personal Licenses in accordance with the Animals (Scientific Procedures) Act 1986,

628 and with the approval of the University of Leeds and Durham University
629 Animal Ethical and Welfare Review Boards.
630
631 **Consent for publication**
632 Not applicable
633
634 **Availability of data and material**
635 The codes used to quantify the CLARITY datasets are made available by
636 author LCA by email request to authors LCA or JD, subject to reference to the
637 current paper. The datasets used and/or analysed during the current study
638 are available from the corresponding author on reasonable request.
639
640 **Competing interests**
641 The authors declare no competing interests.
642
643 **Funding**
644 This work was supported by the Guy's and St. Thomas' Charity Prize PhD
645 scholarship to ALT, a Medical Research Council (UK) grant (G0900625) to
646 SJC and RJR, a University of Leeds Wellcome Trust ISSF (UK) Fellowship, a
647 Royal Society (UK) grant (RG130316), an Alzheimer's Society Fellowship
648 (AS-JF-15-008) to JD, a British Pharmacological Society (UK) grant to JD and
649 CL, a BBSRC grant to LCA (BB/P000479/1) and a BBSRC grant to CL
650 (BB/M008975/1). We acknowledge financial support from the Innovative
651 Medicines Initiative Joint Undertaking under grant agreement no. 115300,
652 resources of which are composed of financial contribution from the European

Union's Seventh Framework Programme (FP7/2007–2013) and EFPIA companies' in kind contribution, the Mortimer D Sackler Foundation and the Sackler Institute for Translational Neurodevelopment (ALT and LCA). Some analysis scripts were provided to ALT at the Computational Image Analysis in Cellular and Developmental Biology course at the Marine Biological Laboratory (Woods Hole, MA, USA), funded by National Institutes of Health (R25 GM103792-01).

Authors' contribution

EP, ALT, LCA and JD conceived the study. EP and ALT performed the experiments. EP, ALT, LCA and JD analysed the data. SJC, RJR, LCA and JD funded the study. All authors contributed to writing the paper. All authors have read and approved the final manuscript.

Acknowledgements

Not applicable.

References

1. Sandin S, Lichtenstein P, Kuja-Halkola R, Larsson H, Hultman CM, Reichenberg A. The familial risk of autism. Jama. 2014;311(17):1770-7.
2. Cardno AG, Gottesman, II. Twin studies of schizophrenia: from bow-and-arrow concordances to star wars Mx and functional genomics. American journal of medical genetics. 2000;97(1):12-7.
3. Ronald A, Happe F, Bolton P, Butcher LM, Price TS, Wheelwright S, et al. Genetic heterogeneity between the three components of the autism spectrum: a twin study. Journal of the American Academy of Child and Adolescent Psychiatry. 2006;45(6):691-9.
4. Ronemus M, Iossifov I, Levy D, Wigler M. The role of de novo mutations in the genetics of autism spectrum disorders. Nature reviews Genetics. 2014;15(2):133-41.
5. Geschwind DH, State MW. Gene hunting in autism spectrum disorder: on the path to precision medicine. The Lancet Neurology. 2015;14(11):1109-20.

685 6. Sahin M, Sur M. Genes, circuits, and precision therapies for autism and
686 related neurodevelopmental disorders. Science. 2015;350(6263).
687 7. Lise MF, El-Husseini A. The neuroligin and neurexin families: from structure
688 to function at the synapse. Cellular and molecular life sciences : CMLS.
689 2006;63(16):1833-49.
690 8. Sudhof TC. Synaptic Neurexin Complexes: A Molecular Code for the Logic
691 of Neural Circuits. Cell. 2017;171(4):745-69.
692 9. Gauthier J, Siddiqui TJ, Huashan P, Yokomaku D, Hamdan FF, Champagne
693 N, et al. Truncating mutations in NRXN2 and NRXN1 in autism spectrum disorders
694 and schizophrenia. Human genetics. 2011;130(4):563-73.
695 10. Mohrmann I, Gillessen-Kaesbach G, Siebert R, Caliebe A, Hellenbroich Y. A
696 de novo 0.57 Mb microdeletion in chromosome 11q13.1 in a patient with speech
697 problems, autistic traits, dysmorphic features and multiple endocrine neoplasia type 1.
698 European journal of medical genetics. 2011;54(4):e461-4.
699 11. Boyle MI, Jespersgaard C, Nazaryan L, Ravn K, Brondum-Nielsen K,
700 Bisgaard AM, et al. Deletion of 11q12.3-11q13.1 in a patient with intellectual
701 disability and childhood facial features resembling Cornelia de Lange syndrome.
702 Gene. 2015;572(1):130-4.
703 12. Li J, Wang L, Gou H, Shi L, Zhang K, Tang M, et al. Targeted sequencing and
704 functional analysis reveal brain-size-related genes and their networks in autism
705 spectrum disorders. Molecular Psychiatry. 2017;22:1282–90.
706 13. Yuan H, Li X, Wang Q, Yang W, Song J, Hu X, et al. A de novo 921Kb
707 microdeletion at 11q13.1 including neurexin 2 in a boy with developmental delay,
708 deficits in speech and language without autistic behaviors. European journal of
709 medical genetics. 2018.
710 14. Williams SM, An JY, Edson J, Watts M, Murigneux V, Whitehouse AJO, et
711 al. An integrative analysis of non-coding regulatory DNA variations associated with
712 autism spectrum disorder. Molecular psychiatry. 2018.
713 15. Wang J, Gong J, Li L, Chen Y, Liu L, Gu H, et al. Neurexin gene family
714 variants as risk factors for autism spectrum disorder. Autism research : official journal
715 of the International Society for Autism Research. 2018;11(1):37-43.
716 16. Duda M, Zhang H, Li HD, Wall DP, Burmeister M, Guan Y. Brain-specific
717 functional relationship networks inform autism spectrum disorder gene prediction.
718 Translational psychiatry. 2018;8(1):56.
719 17. Dachtler J, Glasper J, Cohen RN, Ivorra JL, Swiffen DJ, Jackson AJ, et al.
720 Deletion of alpha-neurexin II results in autism-related behaviors in mice.
721 Translational psychiatry. 2014;4:e484.
722 18. Born G, Grayton HM, Langhorst H, Dudanova I, Rohlmann A, Woodward
723 BW, et al. Genetic targeting of NRXN2 in mice unveils role in excitatory cortical
724 synapse function and social behaviors. Frontiers in synaptic neuroscience. 2015;7:3.
725 19. Dachtler J, Ivorra JL, Rowland TE, Lever C, Rodgers RJ, Clapcote SJ.
726 Heterozygous deletion of alpha-neurexin I or alpha-neurexin II results in behaviors
727 relevant to autism and schizophrenia. Behavioral neuroscience. 2015;129(6):765-76.
728 20. Dudanova I, Tabuchi K, Rohlmann A, Sudhof TC, Missler M. Deletion of
729 alpha-neurexins does not cause a major impairment of axonal pathfinding or synapse
730 formation. The Journal of comparative neurology. 2007;502(2):261-74.
731 21. Beaulieu C. The basis of anisotropic water diffusion in the nervous system - a
732 technical review. NMR in biomedicine. 2002;15(7-8):435-55.

22. Barnea-Goraly N, Kwon H, Menon V, Eliez S, Lotspeich L, Reiss AL. White matter structure in autism: preliminary evidence from diffusion tensor imaging. Biological psychiatry. 2004;55(3):323-6.
23. Noriuchi M, Kikuchi Y, Yoshiura T, Kira R, Shigeto H, Hara T, et al. Altered white matter fractional anisotropy and social impairment in children with autism spectrum disorder. Brain research. 2010;1362:141-9.
24. Belmonte MK, Allen G, Beckel-Mitchener A, Boulanger LM, Carper RA, Webb SJ. Autism and abnormal development of brain connectivity. The Journal of neuroscience : the official journal of the Society for Neuroscience. 2004;24(42):9228-31.
25. Chung K, Wallace J, Kim SY, Kalyanasundaram S, Andalman AS, Davidson TJ, et al. Structural and molecular interrogation of intact biological systems. Nature. 2013;497(7449):332-7.
26. Pervolaraki E, Anderson RA, Benson AP, Hayes-Gill B, Holden AV, Moore BJ, et al. Antenatal architecture and activity of the human heart. Interface focus. 2013;3(2):20120065.
27. Paxinos G, Franklin K. The Mouse Brain in Stereotaxic Coordinates. Third ed: Academic Press; 2008.
28. Pervolaraki E, Dachtler J, Anderson RA, Holden AV. Ventricular myocardium development and the role of connexins in the human fetal heart. Scientific reports. 2017;7(1):12272.
29. Yeh FC, Verstynen TD, Wang Y, Fernandez-Miranda JC, Tseng WY. Deterministic diffusion fiber tracking improved by quantitative anisotropy. PloS one. 2013;8(11):e80713.
30. Basser PJ, Mattiello J, LeBihan D. Estimation of the effective self-diffusion tensor from the NMR spin echo. Journal of magnetic resonance Series B. 1994;103(3):247-54.
31. Jiang H, van Zijl PC, Kim J, Pearlson GD, Mori S. DtiStudio: resource program for diffusion tensor computation and fiber bundle tracking. Computer methods and programs in biomedicine. 2006;81(2):106-16.
32. Ferguson JN, Aldag JM, Insel TR, Young LJ. Oxytocin in the medial amygdala is essential for social recognition in the mouse. The Journal of neuroscience : the official journal of the Society for Neuroscience. 2001;21(20):8278-85.
33. Tanimizu T, Kenney JW, Okano E, Kadoma K, Frankland PW, Kida S. Functional Connectivity of Multiple Brain Regions Required for the Consolidation of Social Recognition Memory. The Journal of neuroscience : the official journal of the Society for Neuroscience. 2017;37(15):4103-16.
34. Emery NJ, Capitanio JP, Mason WA, Machado CJ, Mendoza SP, Amaral DG. The effects of bilateral lesions of the amygdala on dyadic social interactions in rhesus monkeys (Macaca mulatta). Behavioral neuroscience. 2001;115(3):515-44.
35. Rosvold HE, Mirsky AF, Pribram KH. Influence of amygdalectomy on social behavior in monkeys. Journal of comparative and physiological psychology. 1954;47(3):173-8.
36. Mosher CP, Zimmerman PE, Gothard KM. Neurons in the monkey amygdala detect eye contact during naturalistic social interactions. Current biology : CB. 2014;24(20):2459-64.
37. Rutishauser U, Mamelak AN, Adolphs R. The primate amygdala in social perception - insights from electrophysiological recordings and stimulation. Trends in neurosciences. 2015;38(5):295-306.

38. Rutishauser U, Tudusciuc O, Wang S, Mamelak AN, Ross IB, Adolphs R. Single-neuron correlates of atypical face processing in autism. Neuron. 2013;80(4):887-99.
39. Adolphs R, Tranel D, Damasio AR. The human amygdala in social judgment. Nature. 1998;393(6684):470-4.
40. Baron-Cohen S, Ring HA, Bullmore ET, Wheelwright S, Ashwin C, Williams SC. The amygdala theory of autism. Neuroscience and biobehavioral reviews. 2000;24(3):355-64.
41. Maaswinkel H, Baars AM, Gispen WH, Spruijt BM. Roles of the basolateral amygdala and hippocampus in social recognition in rats. Physiology & behavior. 1996;60(1):55-63.
42. Kogan JH, Frankland PW, Silva AJ. Long-term memory underlying hippocampus-dependent social recognition in mice. Hippocampus. 2000;10(1):47-56.
43. Okuyama T, Kitamura T, Roy DS, Itohara S, Tonegawa S. Ventral CA1 neurons store social memory. Science. 2016;353(6307):1536-41.
44. van der Kooij MA, Fantin M, Kraev I, Korshunova I, Grosse J, Zanoletti O, et al. Impaired hippocampal neuroligin-2 function by chronic stress or synthetic peptide treatment is linked to social deficits and increased aggression. Neuropsychopharmacology : official publication of the American College of Neuropsychopharmacology. 2014;39(5):1148-58.
45. Rubin RD, Watson PD, Duff MC, Cohen NJ. The role of the hippocampus in flexible cognition and social behavior. Frontiers in human neuroscience. 2014;8:742.
46. Nicolson R, DeVito TJ, Vidal CN, Sui Y, Hayashi KM, Drost DJ, et al. Detection and mapping of hippocampal abnormalities in autism. Psychiatry research. 2006;148(1):11-21.
47. Schumann CM, Hamstra J, Goodlin-Jones BL, Lotspeich LJ, Kwon H, Buonocore MH, et al. The amygdala is enlarged in children but not adolescents with autism; the hippocampus is enlarged at all ages. The Journal of neuroscience : the official journal of the Society for Neuroscience. 2004;24(28):6392-401.
48. Bachevalier J, Loveland KA. The orbitofrontal-amygdala circuit and self-regulation of social-emotional behavior in autism. Neuroscience and biobehavioral reviews. 2006;30(1):97-117.
49. Beer JS, John OP, Scabini D, Knight RT. Orbitofrontal cortex and social behavior: integrating self-monitoring and emotion-cognition interactions. Journal of cognitive neuroscience. 2006;18(6):871-9.
50. Watson KK, Platt ML. Social signals in primate orbitofrontal cortex. Current biology : CB. 2012;22(23):2268-73.
51. Girgis RR, Minshew NJ, Melhem NM, Nutche JJ, Keshavan MS, Hardan AY. Volumetric alterations of the orbitofrontal cortex in autism. Progress in neuro-psychopharmacology & biological psychiatry. 2007;31(1):41-5.
52. Tyson AL, Hilton ST, Andreae LC. Rapid, simple and inexpensive production of custom 3D printed equipment for large-volume fluorescence microscopy. International journal of pharmaceutics. 2015;494(2):651-6.
53. Herbert MR, Ziegler DA, Deutsch CK, O'Brien LM, Kennedy DN, Filipek PA, et al. Brain asymmetries in autism and developmental language disorder: a nested whole-brain analysis. Brain : a journal of neurology. 2005;128(Pt 1):213-26.
54. Alexander AL, Lee JE, Lazar M, Field AS. Diffusion tensor imaging of the brain. Neurotherapeutics : the journal of the American Society for Experimental NeuroTherapeutics. 2007;4(3):316-29.

55. Alexander AL, Lee JE, Lazar M, Boudos R, DuBray MB, Oakes TR, et al. Diffusion tensor imaging of the corpus callosum in Autism. NeuroImage. 2007;34(1):61-73.
56. Travers BG, Tromp do PM, Adluru N, Lange N, Destiche D, Ennis C, et al. Atypical development of white matter microstructure of the corpus callosum in males with autism: a longitudinal investigation. Molecular autism. 2015;6:15.
57. Ellegood J, Babineau BA, Henkelman RM, Lerch JP, Crawley JN. Neuroanatomical analysis of the BTBR mouse model of autism using magnetic resonance imaging and diffusion tensor imaging. NeuroImage. 2013;70:288-300.
58. Kumar M, Kim S, Pickup S, Chen R, Fairless AH, Ittyerah R, et al. Longitudinal in-vivo diffusion tensor imaging for assessing brain developmental changes in BALB/cJ mice, a model of reduced sociability relevant to autism. Brain research. 2012;1455:56-67.
59. Pitkanen A, Pikkarainen M, Nurminen N, Ylinen A. Reciprocal connections between the amygdala and the hippocampal formation, perirhinal cortex, and postrhinal cortex in rat. A review. Annals of the New York Academy of Sciences. 2000;911:369-91.
60. Cavada C, Company T, Tejedor J, Cruz-Rizzolo RJ, Reinoso-Suarez F. The anatomical connections of the macaque monkey orbitofrontal cortex. A review. Cerebral cortex. 2000;10(3):220-42.
61. Abrams DA, Lynch CJ, Cheng KM, Phillips J, Supekar K, Ryali S, et al. Underconnectivity between voice-selective cortex and reward circuitry in children with autism. Proceedings of the National Academy of Sciences of the United States of America. 2013;110(29):12060-5.
62. Murphy ER, Foss-Feig J, Kenworthy L, Gaillard WD, Vaidya CJ. Atypical Functional Connectivity of the Amygdala in Childhood Autism Spectrum Disorders during Spontaneous Attention to Eye-Gaze. Autism research and treatment. 2012;2012:652408.
63. Sundaram SK, Kumar A, Makki MI, Behen ME, Chugani HT, Chugani DC. Diffusion tensor imaging of frontal lobe in autism spectrum disorder. Cerebral cortex. 2008;18(11):2659-65.
64. Fellgiebel A, Wille P, Muller MJ, Winterer G, Scheurich A, Vucurevic G, et al. Ultrastructural hippocampal and white matter alterations in mild cognitive impairment: a diffusion tensor imaging study. Dementia and geriatric cognitive disorders. 2004;18(1):101-8.
65. Stebbins GT, Murphy CM. Diffusion tensor imaging in Alzheimer's disease and mild cognitive impairment. Behavioural neurology. 2009;21(1):39-49.
66. Carlesimo GA, Cherubini A, Caltagirone C, Spalletta G. Hippocampal mean diffusivity and memory in healthy elderly individuals: a cross-sectional study. Neurology. 2010;74(3):194-200.
67. Ameis SH, Fan J, Rockel C, Voineskos AN, Lobaugh NJ, Soorya L, et al. Impaired structural connectivity of socio-emotional circuits in autism spectrum disorders: a diffusion tensor imaging study. PloS one. 2011;6(11):e28044.
68. Shukla DK, Keehn B, Muller RA. Tract-specific analyses of diffusion tensor imaging show widespread white matter compromise in autism spectrum disorder. Journal of child psychology and psychiatry, and allied disciplines. 2011;52(3):286-95.
69. Jou RJ, Jackowski AP, Papademetris X, Rajeevan N, Staib LH, Volkmar FR. Diffusion tensor imaging in autism spectrum disorders: preliminary evidence of abnormal neural connectivity. The Australian and New Zealand journal of psychiatry. 2011;45(2):153-62.

70. Conturo TE, Williams DL, Smith CD, Gultepe E, Akbudak E, Minshew NJ. Neuronal fiber pathway abnormalities in autism: an initial MRI diffusion tensor tracking study of hippocampo-fusiform and amygdalo-fusiform pathways. Journal of the International Neuropsychological Society : JINS. 2008;14(6):933-46.
71. Stanfield AC, McIntosh AM, Spencer MD, Philip R, Gaur S, Lawrie SM. Towards a neuroanatomy of autism: a systematic review and meta-analysis of structural magnetic resonance imaging studies. European psychiatry : the journal of the Association of European Psychiatrists. 2008;23(4):289-99.
72. Vissers ME, Cohen MX, Geurts HM. Brain connectivity and high functioning autism: a promising path of research that needs refined models, methodological convergence, and stronger behavioral links. Neuroscience and biobehavioral reviews. 2012;36(1):604-25.
73. Rudie JD, Brown JA, Beck-Pancer D, Hernandez LM, Dennis EL, Thompson PM, et al. Altered functional and structural brain network organization in autism. NeuroImage Clinical. 2012;2:79-94.
74. Uddin LQ, Supekar K, Menon V. Reconceptualizing functional brain connectivity in autism from a developmental perspective. Frontiers in human neuroscience. 2013;7:458.
75. Zhan Y, Paolicelli RC, Sforazzini F, Weinhard L, Bolasco G, Pagani F, et al. Deficient neuron-microglia signaling results in impaired functional brain connectivity and social behavior. Nature neuroscience. 2014;17(3):400-6.
76. Missler M, Zhang W, Rohlmann A, Kattenstroth G, Hammer RE, Gottmann K, et al. Alpha-neurexins couple Ca2+ channels to synaptic vesicle exocytosis. Nature. 2003;423(6943):939-48.
77. Alba-Ferrara LM, de Erausquin GA. What does anisotropy measure? Insights from increased and decreased anisotropy in selective fiber tracts in schizophrenia. Frontiers in integrative neuroscience. 2013;7:9.
78. Minshew NJ, Williams DL. The new neurobiology of autism: cortex, connectivity, and neuronal organization. Archives of neurology. 2007;64(7):945-50.
79. Andreae LC, Burrone J. Spontaneous Neurotransmitter Release Shapes Dendritic Arbors via Long-Range Activation of NMDA Receptors. Cell reports. 2015.
80. Ye L, Allen WE, Thompson KR, Tian Q, Hsueh B, Ramakrishnan C, et al. Wiring and Molecular Features of Prefrontal Ensembles Representing Distinct Experiences. Cell. 2016;165(7):1776-88.
81. Jones DK. The effect of gradient sampling schemes on measures derived from diffusion tensor MRI: a Monte Carlo study. Magnetic resonance in medicine. 2004;51(4):807-15.
82. Lebel C, Benner T, Beaulieu C. Six is enough? Comparison of diffusion parameters measured using six or more diffusion-encoding gradient directions with deterministic tractography. Magnetic resonance in medicine. 2012;68(2):474-83.
83. Hasan KM, Parker DL, Alexander AL. Comparison of gradient encoding schemes for diffusion-tensor MRI. Journal of magnetic resonance imaging : JMRI. 2001;13(5):769-80.
84. Yao X, Yu T, Liang B, Xia T, Huang Q, Zhuang S. Effect of increasing diffusion gradient direction number on diffusion tensor imaging fiber tracking in the human brain. Korean journal of radiology. 2015;16(2):410-8.
85. Ni H, Kavcic V, Zhu T, Ekholm S, Zhong J. Effects of number of diffusion gradient directions on derived diffusion tensor imaging indices in human brain. AJNR American journal of neuroradiology. 2006;27(8):1776-81.

931 **Figure Legends**

932 **Figure 1**

933 Quantification of CLARITY imaging. **A** Sections of DTI-scanned brain were
934 segmented at different Bregma levels for (i) the orbitofrontal cortex, (ii) the
935 anterior hippocampus and amygdala, (iii) the mid hippocampus and posterior
936 amygdala and (iv) the posterior hippocampus. **B-D** DTI-scanned brains were
937 computed for tracts. Tissue from wild-type and *Nrxn2α* KO mice were cleared
938 and stained for neurofilament and DAPI (**E**). **F** Automated MATLAB scripts
939 were used to segment the DAPI (blue) and neurofilament (purple) channels
940 such that cell density and axonal density and orientation could be calculated.
941 **G** is representative of a CLARITY-derived 3D stacked image of a DAPI and
942 neurofilament of a region of interest, with **H** being the corresponding
943 segmented image. Scale bar: 100 μm.

944

945 **Figure 2**

946 Deletion of *Nrxn2α* reduces amygdala fractional anisotropy (FA) but not
947 apparent diffusion coefficient (ADC). DTI images of the amygdala was
948 segmented at two regions; anterior (Bregma -1.94 mm) and posterior (Bregma
949 -2.46 mm). FA of the whole amygdala structure was significantly reduced in
950 the posterior (**B**) but not (**A**) region. FA was also significantly reduced in the
951 anterior basolateral amygdala (BLA) (**C**). However, ADC was similar between
952 the genotypes in the anterior (**D**), posterior (**E**) and BLA (**F**). **=P<0.01,
953 *=P<0.05. Error bars represent s.e.m. Wild-type n=6, *Nrxn2α* KO n=6.

954

955 **Figure 3**

956 *Nrxn2α* KO mice have increased apparent diffusion coefficient (ADC) and
957 axial (AD) and radial diffusivity (RD) in the orbitofrontal cortex (OFC) and the
958 anterior cingulate cortex (ACC). Although reduced, there was no significant
959 difference between wild-types and *Nrxn2α* KO mice for FA in the OFC (**A**) and
960 ACC (**C**), but ADC was significantly increased in *Nrxn2α* KO mice in both
961 prefrontal regions (**B** and **D**). The OFC has significantly increased AD and RD
962 (**E-F**), whereas only RD was increased in the ACC (**G-H**). ***=P=0.0005,
963 ***=P<0.001, **=P<0.01, *=P<0.05. Error bars represent s.e.m. Wild-type n=6,
964 *Nrxn2α* KO n=6.
965
966 **Figure 4**
967 Tractographic analysis of amygdala-hippocampus and amygdala-orbitofrontal
968 cortex (OFC) connectivity. Amygdala-hippocampal connections are
969 characterised by greater right hemisphere axial diffusivity (AD) *Nrxn2α* KO
970 mice (**A**) but not radial diffusivity (RD) (**B**). Specific to the BLA, connections to
971 the anterior hippocampus (**C**) and posterior hippocampus (**D**) have greater
972 right hemisphere AD. Although the amygdala-OFC connection was similar
973 between the genotypes for AD (**E**), *Nrxn2α* KO mice had significantly
974 increased RD (**F**). *=P<0.05, ***=P<0.001. Error bars represent s.e.m. Wild-
975 type n=6, Nrxn2α KO n=6.
976
977 **Figure 5**
978 CLARITY reveals differences in axonal alignment and fibre density in *Nrxn2α*
979 KO mice. (**A-C**) Representative images of the CLARITY-treated brain, with
980 ROI defined for the anterior cingulate cortex (ACC), orbitofrontal cortex

981 (OFC), basomedial amygdala (BMA) and basolateral amygdala (BLA). For the
982 ACC, the axonal alignment (**D**) and axon density (**E**) were significantly altered
983 in KO mice, but cell density was unaltered (**F**). Within the medial OFC, only
984 axonal alignment was significantly altered in KOs (**G**), with axon density (**H**)
985 and cell density (**I**) being similar. For the BMA, both the axonal alignment (**J**)
986 and axon density (**K**) were significantly increased, whilst cell density was
987 unaltered (**L**). *=P<0.05, **=P<0.01. Error bars represent s.e.m. Wild-type
988 n=6, *Nrxn2*α KO n=6.
989

The within-subject application of diffusion tensor MRI and CLARITY reveals brain structural changes in *Nrxn2* deletion mice

Supplemental Material

Eleftheria Pervolaraki Ph.D, Adam L. Tyson MRes, Francesca Pibiri Ph.D, Steven L. Poulter Ph.D, Amy C. Reichelt Ph.D, R. John Rodgers Ph.D, Steven J. Clapcote Ph.D, Colin Lever Ph.D, Laura C. Andreae M.D. Ph.D, James Dachtler Ph.D

Supplemental Materials and Methods

Diffusion Tensor MRI

Data Acquisition

Brain MR imaging was performed on a vertical 9.4 Tesla spectrometer (Bruker AVANCE II NMR, Ettlingen, Germany) with an 89 mm wide bore, 3 radio frequency channels with digital broadband frequency synthesis (6-620 MHz) and an imaging coil with diameter of 25 mm for hydrogen (1H). 3D images for each brain were obtained using a DT-MRI protocol (TE: 35 ms, TR: 700 ms, 10 signal averages). The field of view was set at 128 x 128 x 128, with a cubic resolution of 100 μm/pixel and a b value of 1200 s/mm^2. For each brain, diffusion weighted images were obtained in 6 directions, based upon recent published protocols (1-5). The subject of the number of diffusions gradients has been debated (6), with studies suggesting limited benefits of using more than 6 directions in biological tissue (7-9). The imaging time for each brain was 60 hours.

CLARITY

Solutions:

Hydrogel solution: 2% PFA 2% acrylamide 0.05% bis-acrylamide and 0.25% VA-044 thermal initiator (2,2'-Azobis[2-(2-imidazolin-2-yl) propane] dihydrochloride) in PBS, pH 7.4.

Clearing buffer: 8% Sodium dodecyl sulfate in 200mM boric acid, pH 8.5.

Multiphoton imaging – methodological outline

Cleared samples were mounted in custom 3D printed chambers for two-photon imaging. Images were acquired using ZEN Black (Zeiss, Germany). DAPI signal was detected using a 485 nm short pass filter, and neurofilament using a 500-550 nm band pass filter. The power of the excitation laser was varied to maximise the dynamic range for each image, but all other parameters were kept constant. The images were analysed using custom MATLAB (version 9.1, The Mathworks Inc.) scripts. Two-dimensional images were visualised using ImageJ (10) and three-dimensional images using Vaa3D (11).

Multiphoton imaging and analysis – image analysis method

Pre-processing

Image files were loaded into MATLAB (The Mathworks Ltd.) using the BioFormats toolbox (12), and the raw image data were obtained along with the precise voxel dimensions from the metadata. Each two-dimensional (2D) image from the three-dimensional (3D) stack was initially corrected for uneven background illumination by element-wise division by a 2D reference image. This reference image was calculated as the mean 2D image through the 3D stack, which was smoothed using a 2D Gaussian kernel with a full-width at half maximum (FWHM) of 20 % of the geometric mean of the dimensions of the 2D image (mean dimension). The image was denoised by filtering the image with a Gaussian kernel with a standard deviation of one pixel. Background subtraction was carried out by subtracting a smoothed, filtered image (FWHM 10 % of the mean dimension). Each pixel was then smoothed using a 3D Gaussian kernel with FWHM of 1.5 μm (the largest axonal diameter expected according to Perge et al. (13).

Segmentation

The numerical gradient of the image in each dimension $(\Delta X, \Delta Y, \Delta Z)$ was calculated, and these were combined to calculate the magnitude of the gradient $\left(\sqrt{\Delta X^2 + \Delta Y^2 + \Delta Z^2}\right)$. The resulting image was thresholded, using a combination of the Otsu (1979) and Rosin (2001) methods (Rosin threshold + 2/5 Otsu threshold) (14, 15). The gradient image highlights the edge of each axon; to combine these into a single object, the image was dilated and then eroded with a cubic structuring element (each side being 1.5 μm, to 'close' the largest axons as per Perge et al. (13)). Very small objects (less than 50 μm^3) were removed from the image as they reflected noise, very small neuronal processes and gradients around cells.

Owing to variations in staining intensity of different axons, the thresholding produced segmented axons of various thicknesses that did not necessarily reflect the true structure. To remove this bias, the thresholded image was skeletonised using a homotopic thinning algorithm (16) implemented in MATLAB(17). The resulting image was dilated and then eroded using a cubic structuring element (10 pixels on each side for dilation, 9 for erosion) to produce connected processes with a uniform two-pixel diameter. This dilation ensured that the voxels in the binary image were connected via their faces (6-connected) rather than just their corners (26-connected), which better reflects the true structure of biological processes. This method detects

most large axons at the expense of smaller processes, and the loss of any information about axon diameter. These steps are outlined in Supp. Figure 2.

Analysis

The density of axons was calculated as the fraction of the image volume taken up by the segmented axons. A measure of axonal alignment was calculated by determining the mean axonal alignment along each dimension. This alignment was calculated by moving along the 3D image in a single dimension, keeping the coordinates in the other dimensions constant, and counting the number of times the pixel intensity did not change (i.e. how many times an axon was not entered or left). This number was averaged across each face of the image volume and scaled to the length of each dimension to produce a metric of how constant the image intensity is in that dimension. The perfect case of no intensity change (i.e. all axons are aligned perfectly with a particular dimension) gives a value of 1. The greater the difference between this measure in each three dimensions, the more aligned the axons must be (i.e. their directions are anisotropic). The standard deviation of this measure across the three dimensions was calculated as the axonal alignment.

The alignment calculation is illustrated in Supp. Figure 3 for a simple, two-dimensional case. Supp. Figure 3a shows the case of low axonal alignment, and Supp. Figure 3b shows the case of high axonal alignment. In each case, for illustration, each pixel represented by a small square on the grid is classed as either containing an axon or not. In the real images, the pixels are smaller, and are actually binary. In each axis, the number of pixel transitions in which the presence of an axon does not change is divided by the number of transitions, and the average is calculated. The standard deviation of this average for all axes is the measure of axonal alignment. When the alignment is low, the two averages are similar, and the standard deviation is low. When the alignment is high the two averages are very different, and the standard deviation is high. To analyse the real data, this same calculation is carried out in 3D, but in a much larger grid of voxels. Cell density was calculated as the number of cells per mm^3.

Supp. Table 1

Brain Region	DTI Measure	ANOVA Comparison	F Value	P Value
Anterior Hippocampus	FA	Genotype	$F_{(1,10)} = 3.91$	P = 0.063
		Hemisphere	$F_{(1,10)} = 3.89$	P = 0.065
Mid Hippocampus	FA	Genotype	$F_{(1,10)} = 3.12$	P = 0.07
		Hemisphere	$F_{(1,10)} <1$	P = 0.146
Posterior Hippocampus	FA	Genotype	$F_{(1,10)} = 1.99$	P = 0.104
		Hemisphere	$F_{(1,10)} = 1.95$	P = 0.101
Anterior Hippocampus	ADC	Genotype	$F_{(1,10)} = 3.17$	P = 0.073
		Hemisphere	$F_{(1,10)} = 2.20$	P = 0.095
Mid Hippocampus	ADC	Genotype	$F_{(1,10)} <1$	P = 0.160
		Hemisphere	$F_{(1,10)} = 1.62$	P = 0.115
Posterior Hippocampus	ADC	**Genotype**	**$F_{(1,10)} = 8.88$**	**P = 0.036**
		Hemisphere	$F_{(1,10)} <1$	P = 0.180
Anterior Hippocampus	AD	Genotype	$F_{(1,10)} <1$	P = 0.187
		Hemisphere	$F_{(1,10)} = 1.07$	P = 0.121
Mid Hippocampus	AD	Genotype	$F_{(1,10)} <1$	P = 0.153
		Hemisphere	$F_{(1,10)} = 1.04$	P = 0.124
Posterior Hippocampus	AD	Genotype	$F_{(1,10)} = 3.45$	P = 0.07
		Hemisphere	**$F_{(1,10)} = 6.19$**	P = 0.052
Anterior Hippocampus	RD	Genotype	$F_{(1,10)} = 3.03$	P = 0.086
		Hemisphere	$F_{(1,10)} <1$	P = 0.137
Mid Hippocampus	RD	Genotype	$F_{(1,10)} <1$	P = 0.140
		Hemisphere	$F_{(1,10)} = 1.33$	P = 0.119
Posterior Hippocampus	RD	**Genotype**	**$F_{(1,10)} = 10.83$**	**P = 0.027**
		Hemisphere	$F_{(1,10)} = 3.48$	P = 0.07

Statistical analysis of the anterior (Bregma -1.94 mm), mid (Bregma -2.46 mm) and posterior (Bregma -3.28 mm) hippocampus for fractional anisotropy (FA), apparent diffusion coefficient (ADC), axial diffusion (AD) and radial diffusion (RD). Analysis was performed using repeated measure two-way ANOVAs for genotype and hemisphere (Benjamini-Hochberg corrected (corrected P values stated)).

Supp. Table 2

Brain Region	DTI Measure	ANOVA Comparison	F Value	P Value
Amygdala-Anterior Hippocampus	AD	Genotype	$F_{(1,10)} <1$	P = 0.164
		Hemisphere	$F_{(1,10)} = 2.10$	P = 0.097
		Genotype x Hemisphere	**$F_{(1,10)} = 12.12$**	**P = 0.023**
Amygdala-Anterior Hippocampus	RD	Genotype	$F_{(1,10)} <1$	P = 0.149
		Hemisphere	$F_{(1,10)} = 1.32$	P = 0.106
		Genotype x Hemisphere	$F_{(1,10)} <1$	P = 0.155
Amygdala-Posterior Hippocampus	AD	Genotype	$F_{(1,10)} <1$	P = 0.142
		Hemisphere	$F_{(1,10)} <1$	P = 0.189
		Genotype x Hemisphere	$F_{(1,10)} = 4.54$	P = 0.061
Amygdala-Posterior Hippocampus	RD	Genotype	$F_{(1,10)} <1$	P = 0.151
		Hemisphere	$F_{(1,10)} <1$	P = 0.135
		Genotype x Hemisphere	$F_{(1,10)} <1$	P = 0.128
BLA-Anterior Hippocampus	AD	Genotype	$F_{(1,10)} <1$	P = 0.167
		Hemisphere	**$F_{(1,10)} = 6.59$**	**P = 0.047**
		Genotype x Hemisphere	**$F_{(1,10)} = 10.53$**	**P = 0.032**
BLA-Anterior Hippocampus	RD	Genotype	$F_{(1,10)} <1$	P = 0.158
		Hemisphere	$F_{(1,10)} = 2.59$	P = 0.092
		Genotype x Hemisphere	$F_{(1,10)} <1$	P = 0.173
BLA-Posterior Hippocampus	AD	Genotype	$F_{(1,10)} <1$	P = 0.169
		Hemisphere	**$F_{(1,10)} = 12.79$**	**P = 0.018**
		Genotype x Hemisphere	**$F_{(1,10)} = 12.97$**	**P = 0.02**
BLA-Posterior Hippocampus	RD	Genotype	$F_{(1,10)} <1$	P = 0.162
		Hemisphere	$F_{(1,10)} = 3.11$	P = 0.077
		Genotype x Hemisphere	$F_{(1,10)} <1$	P = 0.178

Statistical analysis of the anterior (Bregma -1.94 mm), and posterior (Bregma -3.28 mm) amygdala-hippocampal connections, analysed for axial diffusion (AD) and radial diffusion (RD). Analysis was performed using repeated measure two-way ANOVAs for genotype and hemisphere (Benjamini-Hochberg corrected (corrected P values stated)).

Supp. Table 3

Brain Region	CLARITY Measure	ANOVA Comparison	F Value	P Value
M1	OI	Genotype	$F_{(1,10)} <1$	P = 0.182
		Hemisphere	$F_{(1,10)} = 1.74$	P = 0.108
M1	Cell Density	Genotype	$F_{(1,10)} = 2.04$	P = 0.099
		Hemisphere	$F_{(1,10)} = 1.41$	P = 0.117
M1	Fibre Density	Genotype	$F_{(1,10)} <1$	P = 0.171
		Hemisphere	$F_{(1,10)} <1$	P = 0.176
S1	OI	Genotype	$F_{(1,10)} <1$	P = 0.185
		Hemisphere	$\mathbf{F_{(1,10)} = 36.86}$	**P = 0.005**
S1	Cell Density	Genotype	$F_{(1,10)} <1$	P = 0.131
		Hemisphere	$\mathbf{F_{(1,10)} = 13.73}$	**P = 0.016**
S1	Fibre Density	Genotype	$F_{(1,10)} = 1.73$	P = 0.110
		Hemisphere	$\mathbf{F_{(1,10)} = 8.51}$	**P = 0.038**
BF	OI	Genotype	$F_{(1,10)} <1$	P = 0.191
		Hemisphere	$\mathbf{F_{(1,10)} = 10.59}$	**P = 0.034**
BF	Cell Density	Genotype	$F_{(1,10)} <1$	P = 0.133
		Hemisphere	$\mathbf{F_{(1,10)} = 8.70}$	**P = 0.041**
BF	Fibre Density	Genotype	$F_{(1,10)} <1$	P = 0.144
		Hemisphere	$F_{(1,10)} <1$	P = 0.126

Statistical analysis of the primary motor cortex (M1), primary somatosensory cortex (S1) and the barrel field (BF). CLARITY imaged regions were then analysed for orientation index (OI), cell density and fibre density. Analysis was performed using repeated measure two-way ANOVAs for genotype and hemisphere (Benjamini-Hochberg corrected (corrected P values stated)).

Supp. Figure 1

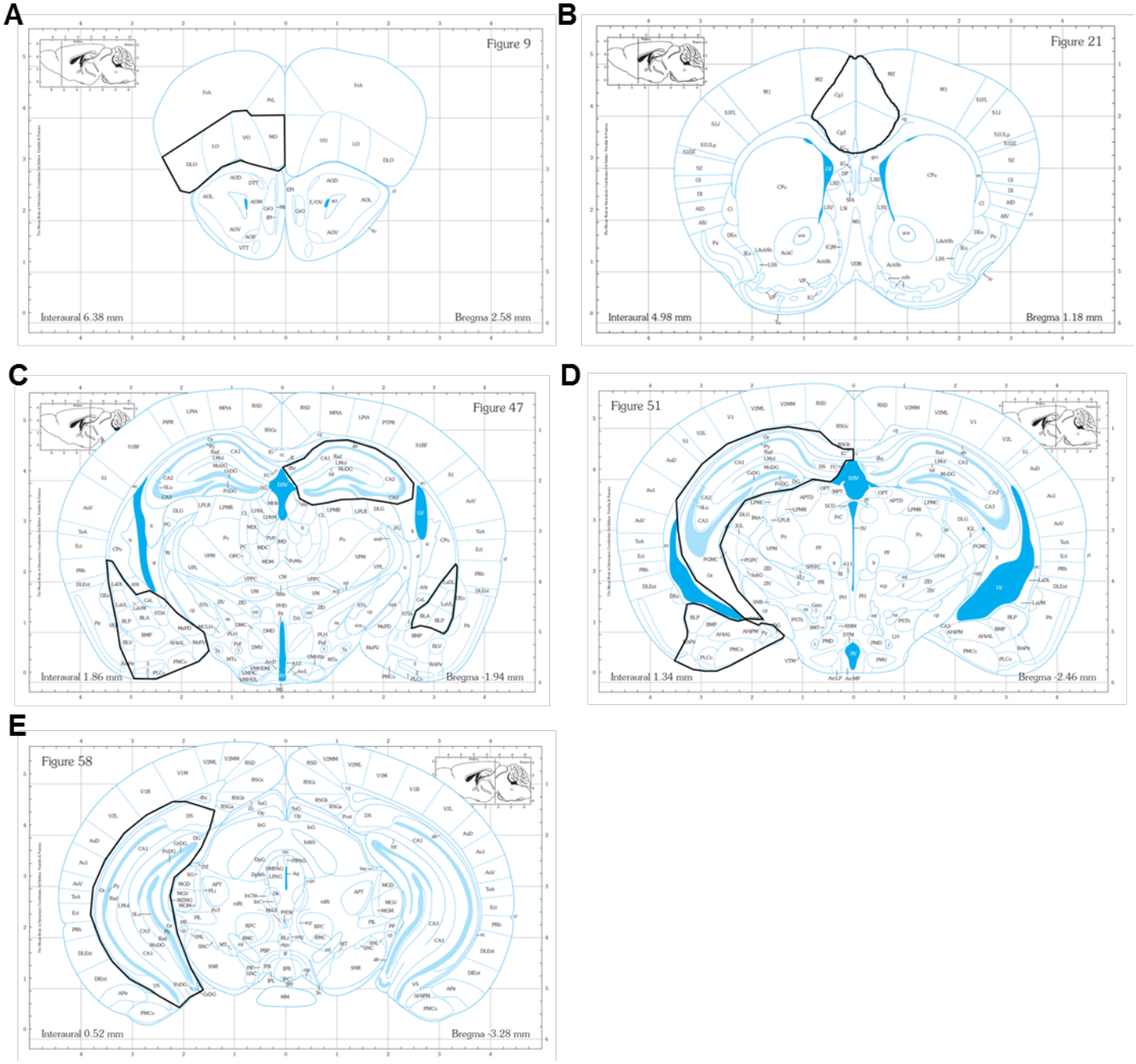

Atlas maps representing manual segmentation of regions of interest (ROI). (**A**) The orbitofrontal cortex ROI. (**B**) The ACC ROI. (**C**) The anterior hippocampus, anterior amygdala and basolateral amygdala ROI. (**D**) The mid hippocampus and posterior amygdala ROI. (**E**) The posterior hippocampus ROI. The atlas maps were used with the permission of the Authors (18).

Supp. Figure 2

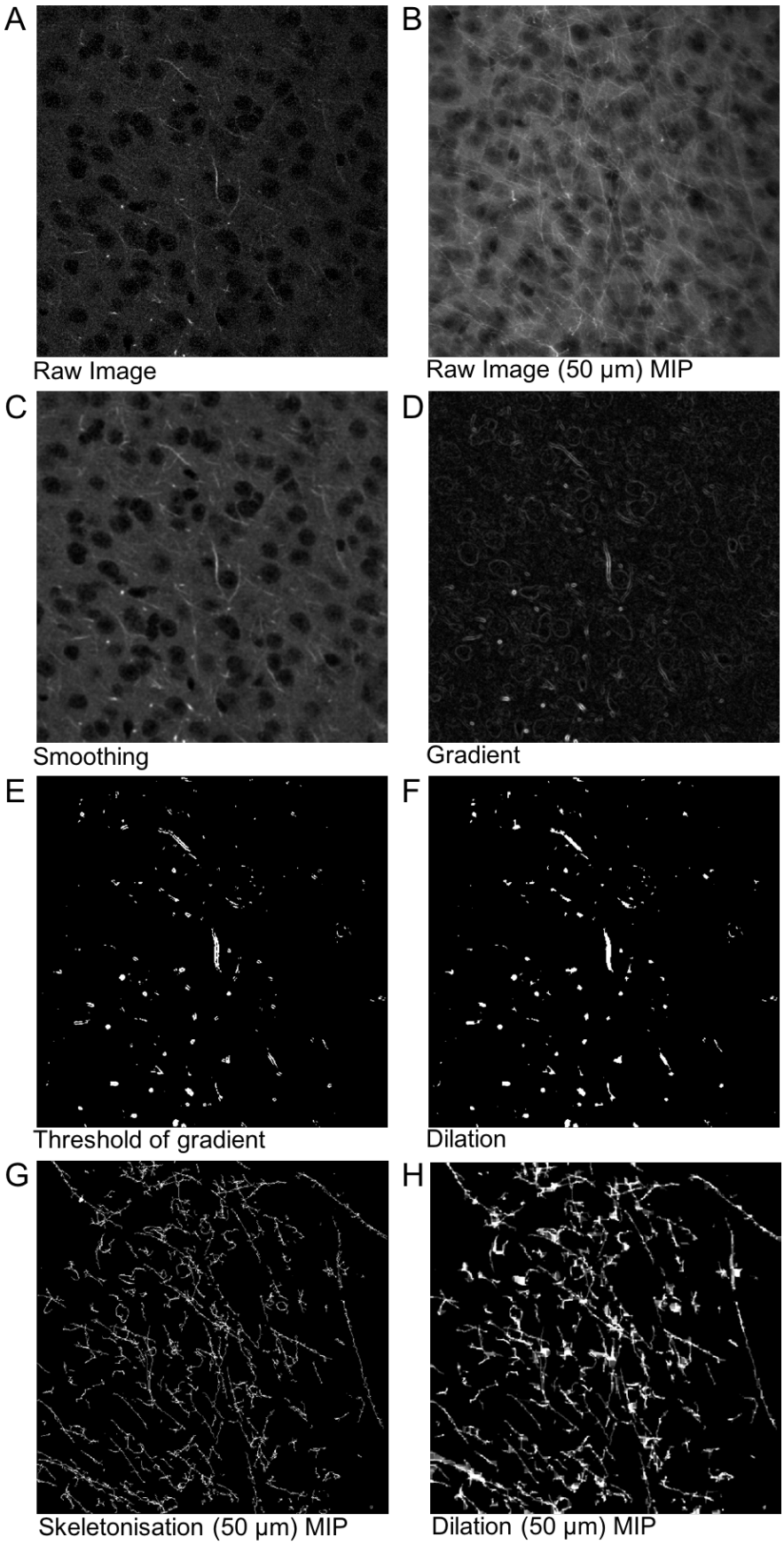

Analysis methodology of axonal segmentation from multiphoton images.

Supp. Figure 3

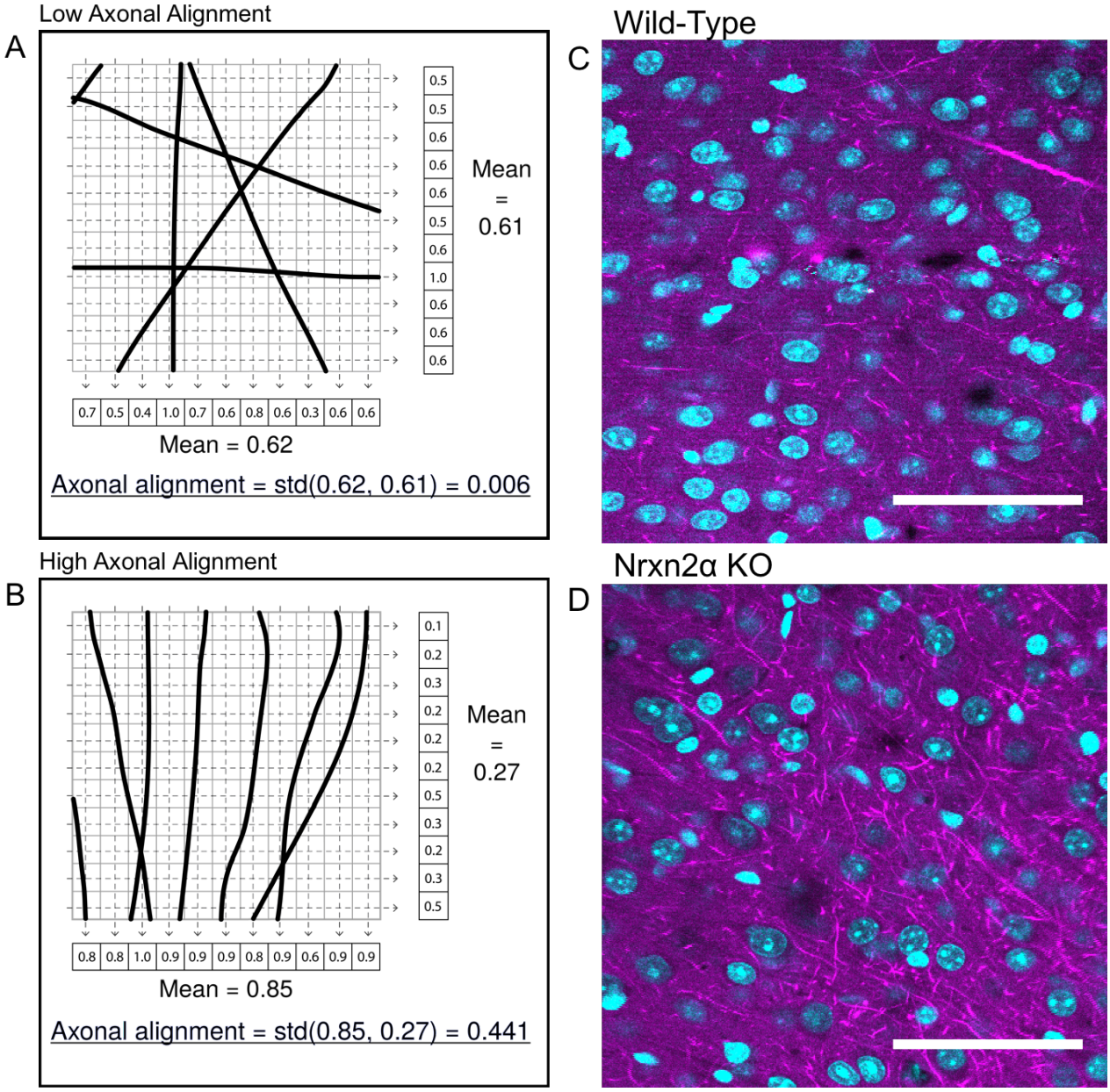

A and B. Illustration of the axonal alignment calculation in a simple two-dimensional case. The grey grid represents the image pixels, the black lines axons and the dashed lines represent the calculation process. Standard deviation denoted as std. **C and D.** Cingulate cortex images taken from wild-type and Nrxn2α KO mice, visually representing the greater axonal alignment and density in KO mice.

Supp. Figure 4

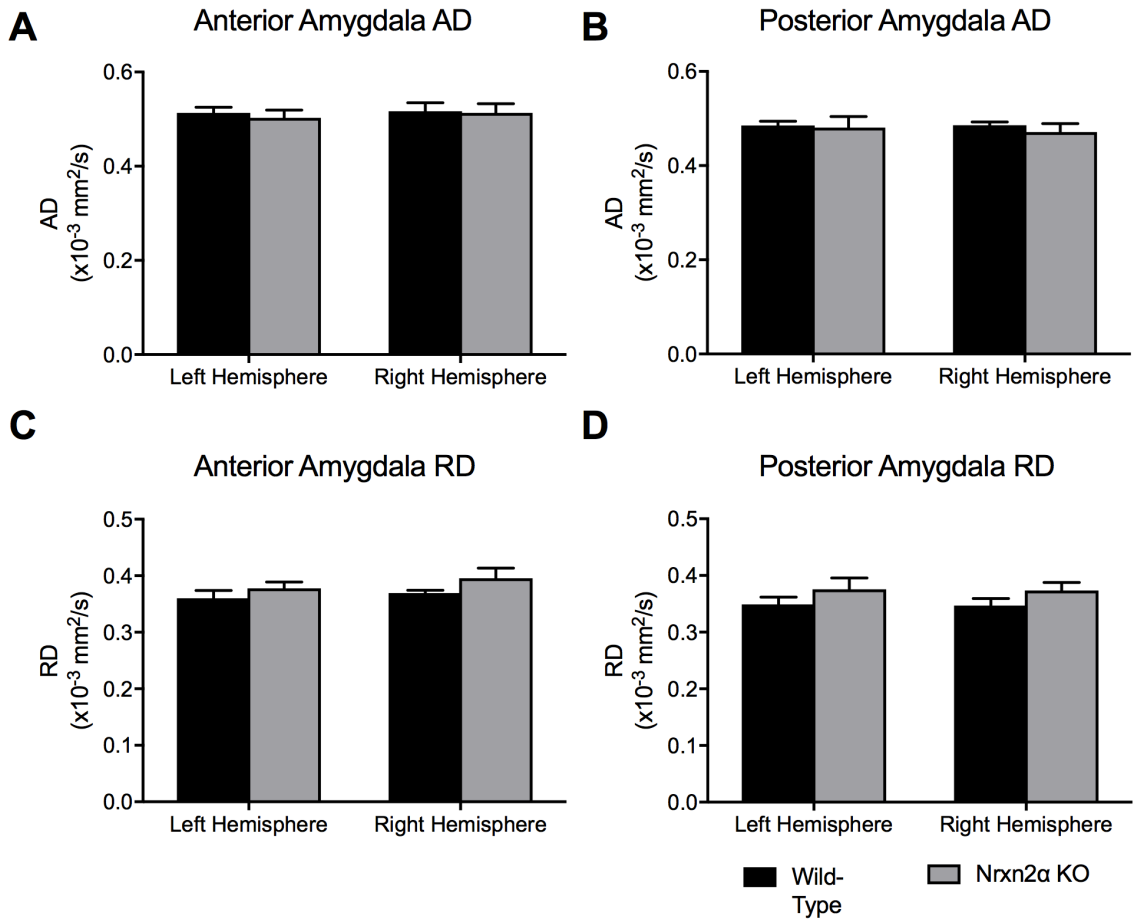

Axial diffusivity (AD) and radial diffusivity (RD) in the amygdala. The entire amygdala was segmented from DTI images at two regions; anterior (**A** and **C**: Bregma -1.94 mm) and posterior (**B** and **D**: Bregma -2.46 mm). No significant differences were observed between the genotypes for anterior or posterior regions. Error bars represent s.e.m. Wild-type n=6, Nrxn2α KO n=6.

Supp. Figure 5

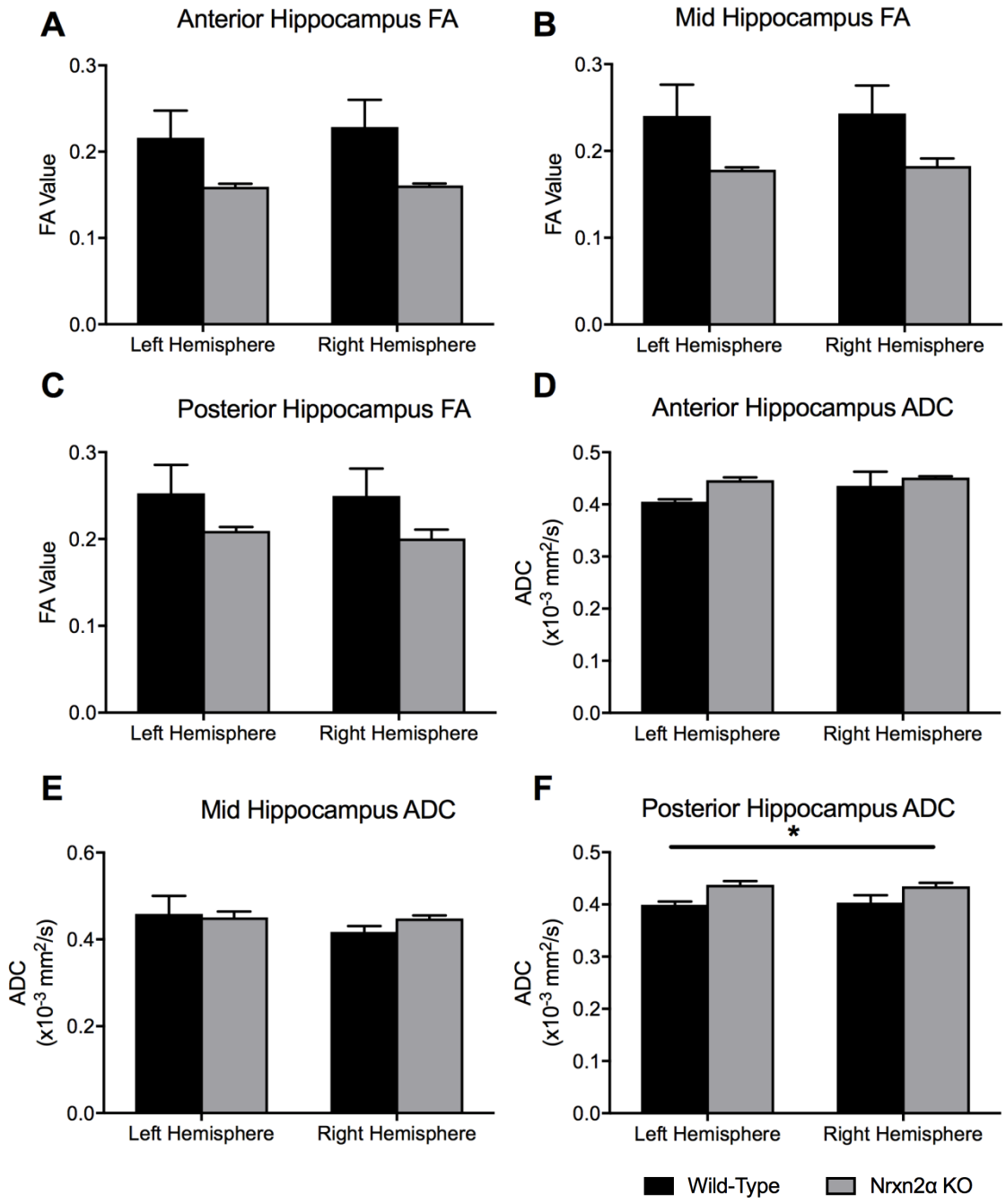

Fractional anisotropy (FA) and apparent diffusion coefficient (ADC) of the anterior to posterior hippocampus. Although Nrxn2α KO had trends towards lower FA in the anterior (**A**), mid (**B**) and posterior (**C**) hippocampus, there were no significant differences. Similarly, anterior (**D**) and mid (**E**) hippocampal regions did not vary between the genotypes, the posterior hippocampus (**F**) had significantly increased ADC (f). * = $P<0.05$. Error bars represent s.e.m. Wild-type n=6, Nrxn2α KO n=6.

Supp. Figure 6

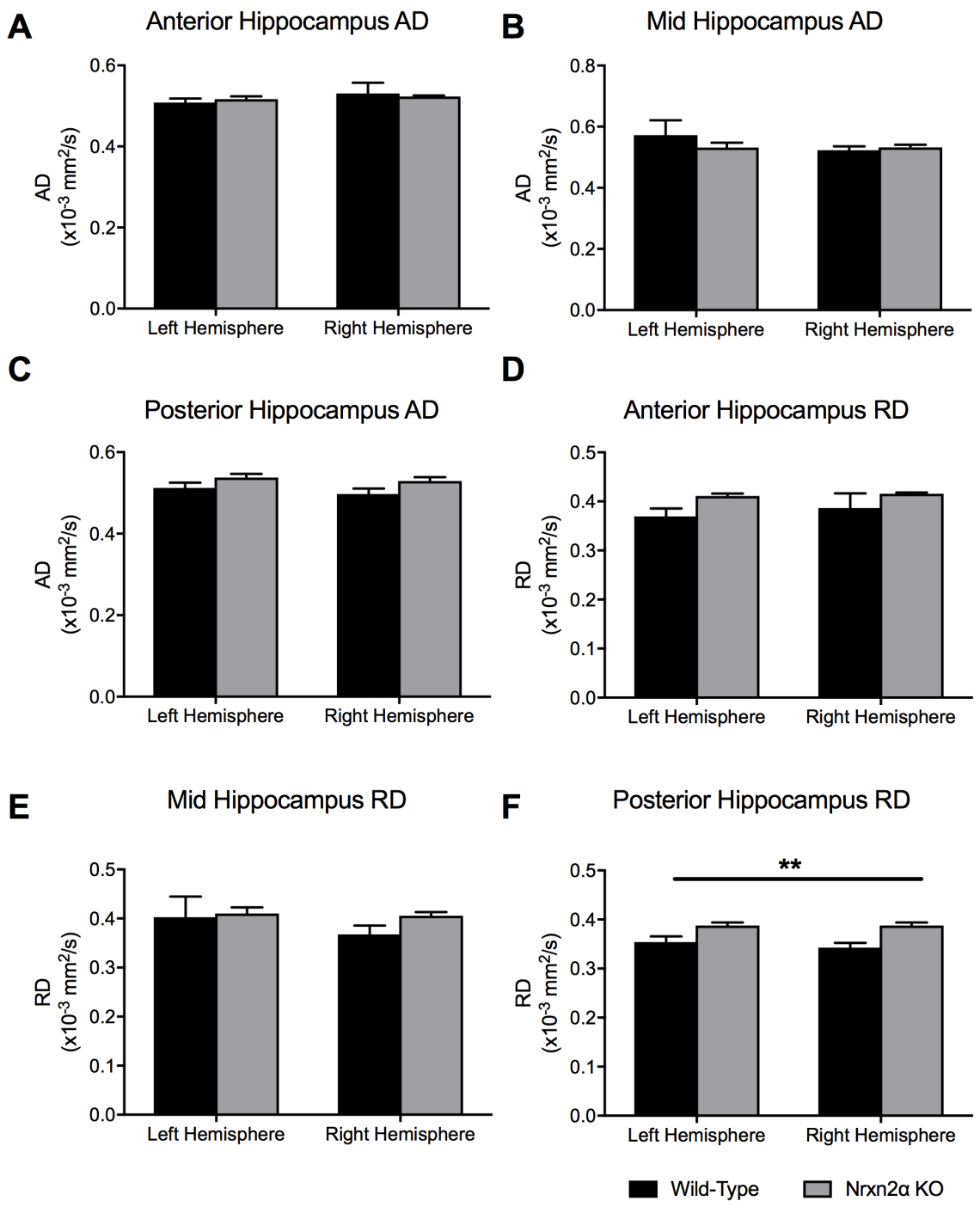

Axial diffusivity (AD) and radial diffusivity (RD) of the anterior to posterior hippocampus. AD did not differ in either the anterior (**A**), mid (**B**) and posterior (**C**) hippocampus. Although the anterior (**D**) and mid (**E**) hippocampal regions did not vary between the genotypes, the posterior hippocampus (**F**) had significantly increased RD (f). ** = P<0.01. Error bars represent s.e.m. Wild-type n=6, Nrxn2α KO n=6.

Supp. Figure 7

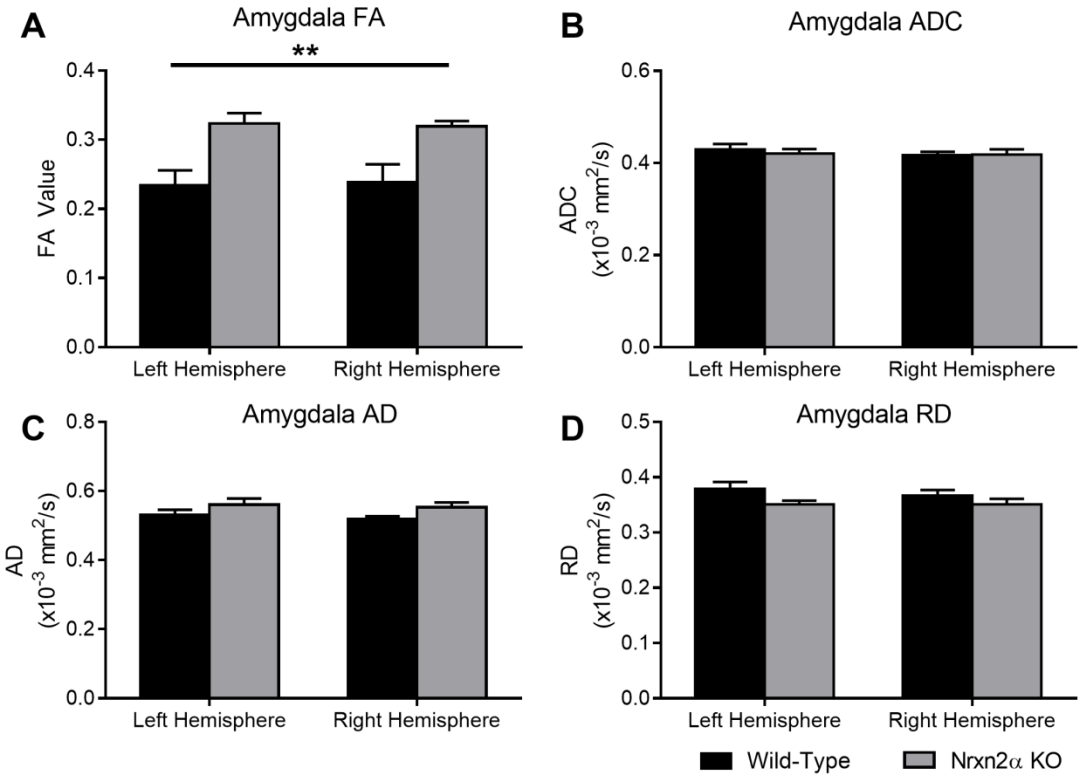

DTI quantified for the whole amygdala volume. (**A**) Fractional anisotropy (FA) was significantly increased in Nrxn2α KO mice (genotype: $F_{(1,10)} = 11.15$, $p = 0.008$). However, (**B**) apparent diffusion coefficient (ADC) was not significantly altered (genotype: $F_{(1,10)} <1$, $p = 0.782$), nor was (**C**) axial diffusivity (AD) (genotype: $F_{(1,10)} = 3.06$, $p = 0.111$) or (**D**) radial diffusivity (RD) (genotype: $F_{(1,10)} = 2.47$, $p = 0.147$). Error bars represent s.e.m. ** = $P<0.01$. Wild-type n=6, Nrxn2α KO n=6.

Supp. Figure 8

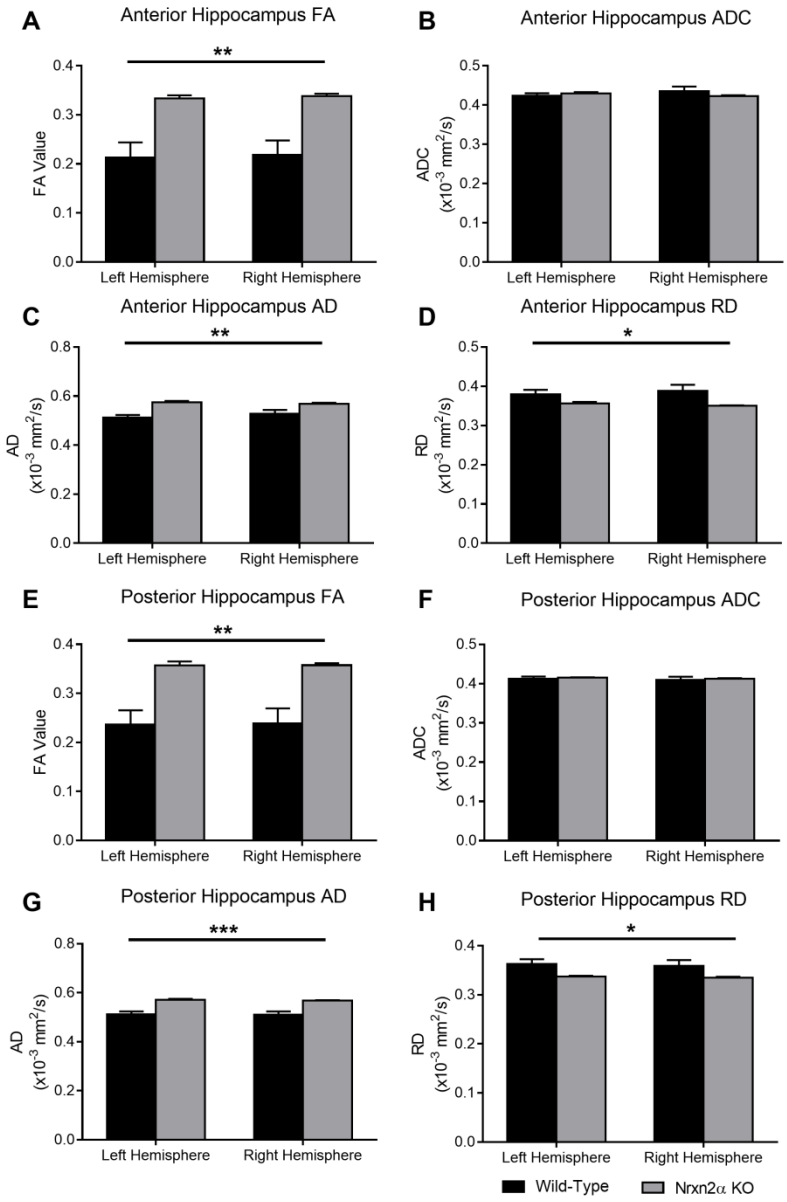

DTI quantified for the whole anterior hippocampus (Bregma -1.06 mm – -2.46 mm) and posterior hippocampus (Bregma -2.54 mm – -3.16 mm). (**A**) Fractional anisotropy (FA) in the anterior hippocampus was significantly increased in Nrxn2α KO mice (genotype: $F_{(1,10)} = 15.63$, $p = 0.0027$) but (**B**) apparent diffusion coefficient (ADC) was not altered (genotype: $F_{(1,10)} <1$, $p = 0.738$). (**C**) Axial diffusivity (AD) (genotype: $F_{(1,10)} = 16.17$, $p = 0.0024$) and (**D**) radial diffusivity (RD) (genotype: $F_{(1,10)} = 5.05$, $p = 0.048$) were both significantly altered in Nrxn2α KO mice. In the posterior hippocampus, in Nrxn2α KO mice, (**E**) FA was significant increased (genotype: $F_{(1,10)} = 15.62$, $p = 0.0027$), (**F**) ADC was similar to wild-types (genotype: $F_{(1,10)} <1$, $p = 0.679$), (**G**) AD was increased (genotype: $F_{(1,10)} = 22.31$, $p = 0.0008$) and (**H**) RD was significantly reduced (genotype: $F_{(1,10)} = 5.34$, $p = 0.043$). Error bars represent s.e.m. * = P<0.05, ** = P<0.01, *** = P<0.001. Wild-type n=6, Nrxn2α KO n=6.

Supp. Figure 9

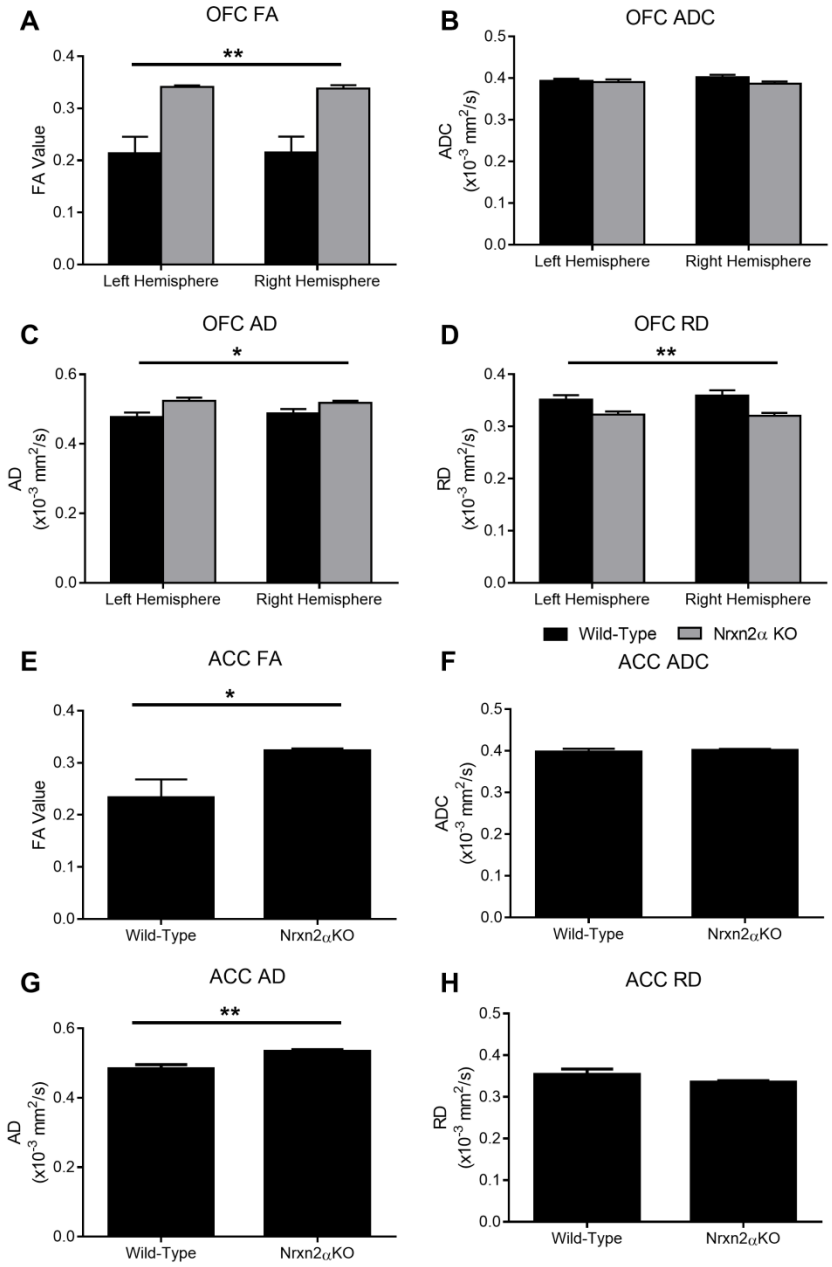

DTI quantified for the whole orbitofrontal cortex (OFC) and anterior cingulate cortex (ACC) and posterior hippocampus (Bregma -1.34 mm – -0.46 mm). (**A**) Fractional anisotropy (FA) in the OFC was significantly increased in Nrxn2α KO mice (genotype: $F_{(1,10)} = 16.14$, $p = 0.0024$) but (**B**) apparent diffusion coefficient (ADC) was not altered (genotype: $F_{(1,10)} = 1.43$, $p = 0.260$). (**C**) Axial diffusivity (AD) (genotype: $F_{(1,10)} = 6.71$, $p = 0.027$) and (**D**) radial diffusivity (RD) (genotype: $F_{(1,10)} = 10.07$, $p = 0.0099$) were both significantly altered in Nrxn2α KO mice. In the ACC of Nrxn2α KO mice, (**E**) FA was significant increased (genotype: $t_{(10)} = 2.55$, $p = 0.029$), (**F**) ADC was similar to wild-types (genotype: $t_{(10)} = 2.55$, $p = 0.618$), (**G**) AD was increased (genotype: $t_{(10)} = 3.89$, $p = 0.003$) and (**H**) RD was not significantly different (genotype: $t_{(10)} = 1.35$, $p = 0.208$). Error bars represent s.e.m. * = $P<0.05$, ** = $P<0.01$. Wild-type n=6, Nrxn2α KO n=6.

Supp. Figure 10

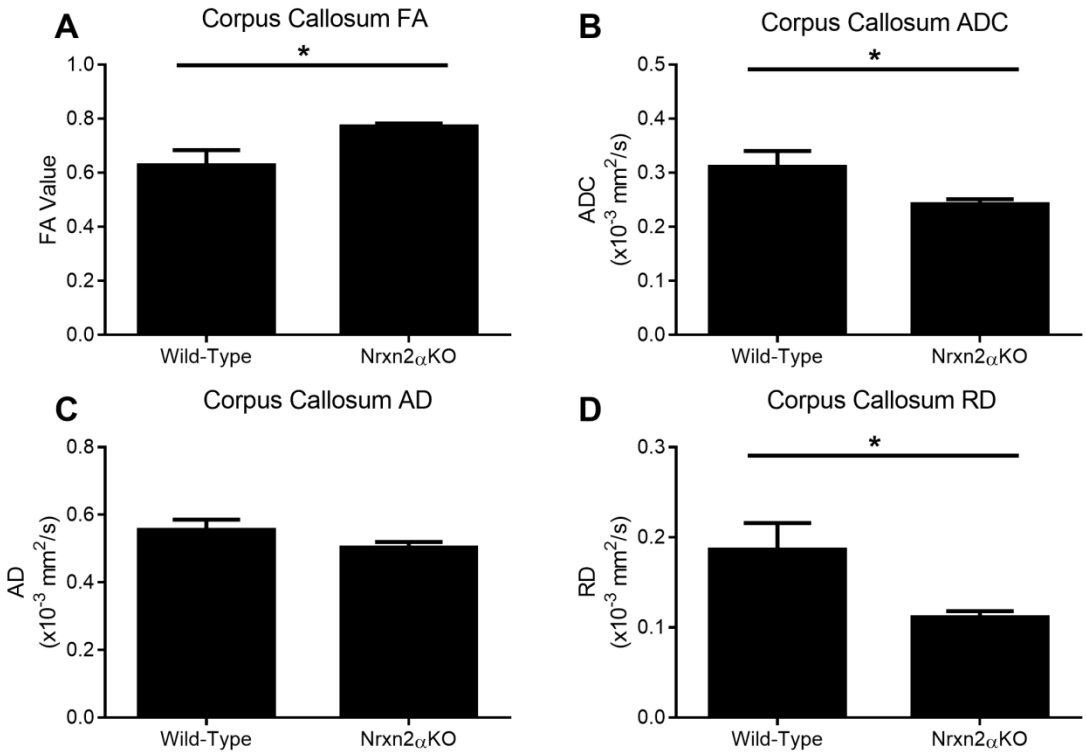

DTI quantification of the corpus callosum (Bregma 0.98 mm). To examine the integrity of white matter tracts within Nrxn2α KO mice, we examined diffusivity in the corpus callosum. (**A**) Fractional anisotropy (FA) was significantly increased in Nrxn2α KO mice (genotype: $t_{(10)} = 2.50$, $p = 0.032$) and apparent diffusion coefficient (ADC) (**B**) significantly decreased (genotype: $t_{(10)} = 2.28$, $p = 0.046$). This difference appeared to be driven predominantly by radial diffusivity (RD), as axial diffusion (AD) (**C**) was not significantly different (genotype: $t_{(10)} = 1.49$, $p = 0.168$) whilst RD (**D**) was significantly reduced in Nrxn2α KO mice (genotype: $t_{(10)} = 2.45$, $p = 0.034$). Error bars represent s.e.m. * = $P<0.05$. Wild-type n=6, Nrxn2α KO n=6.

Supp. Figure 11

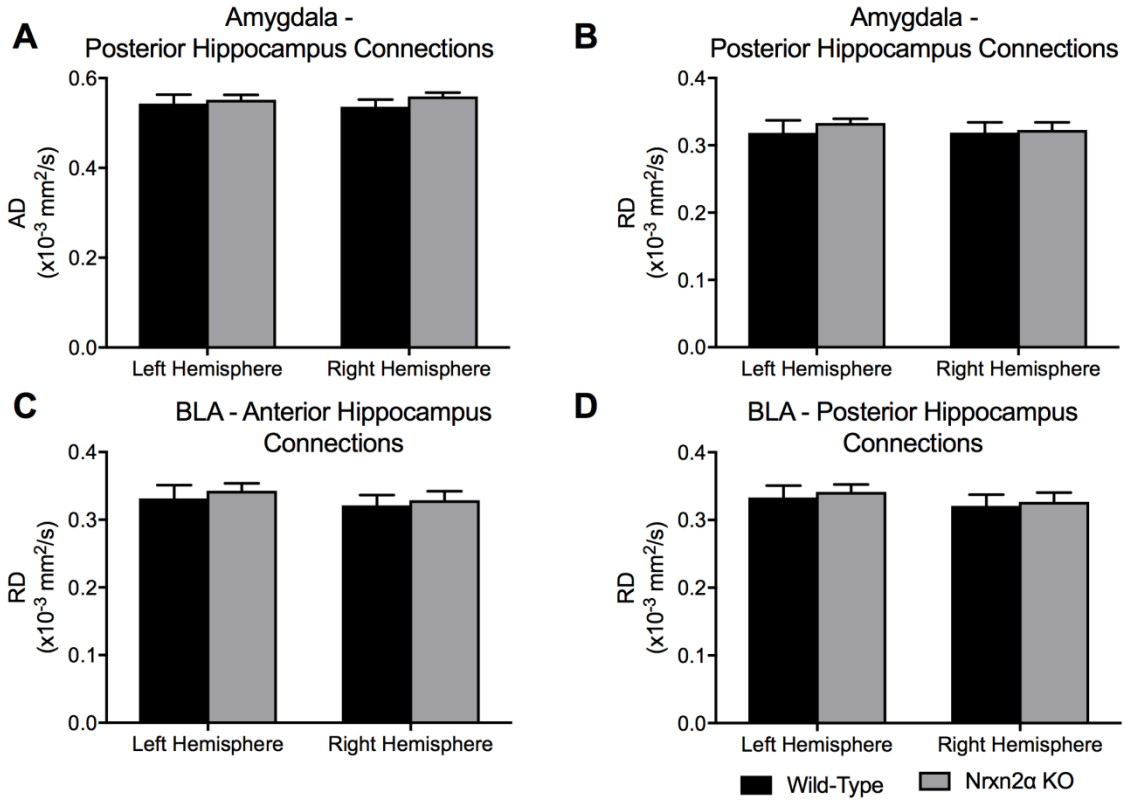

Axial diffusivity (AD) and radial diffusivity (RD) of computed tracts of connections from the amygdala to hippocampus. Tracts from the anterior amygdala to the posterior hippocampus (Bregma -2.46 mm) were analysed for AD (**A**) and RD (**B**). No significant differences between the tracts of Nrxn2α KO mice were observed. No significant differences were found for RD of tracts specifically from the basolateral nuclei of the amygdala (BLA) to the anterior (**C**) or posterior (**D**) hippocampus. Error bars represent s.e.m. Wild-type n=6, Nrxn2α KO n=6.

Supp. Figure 12

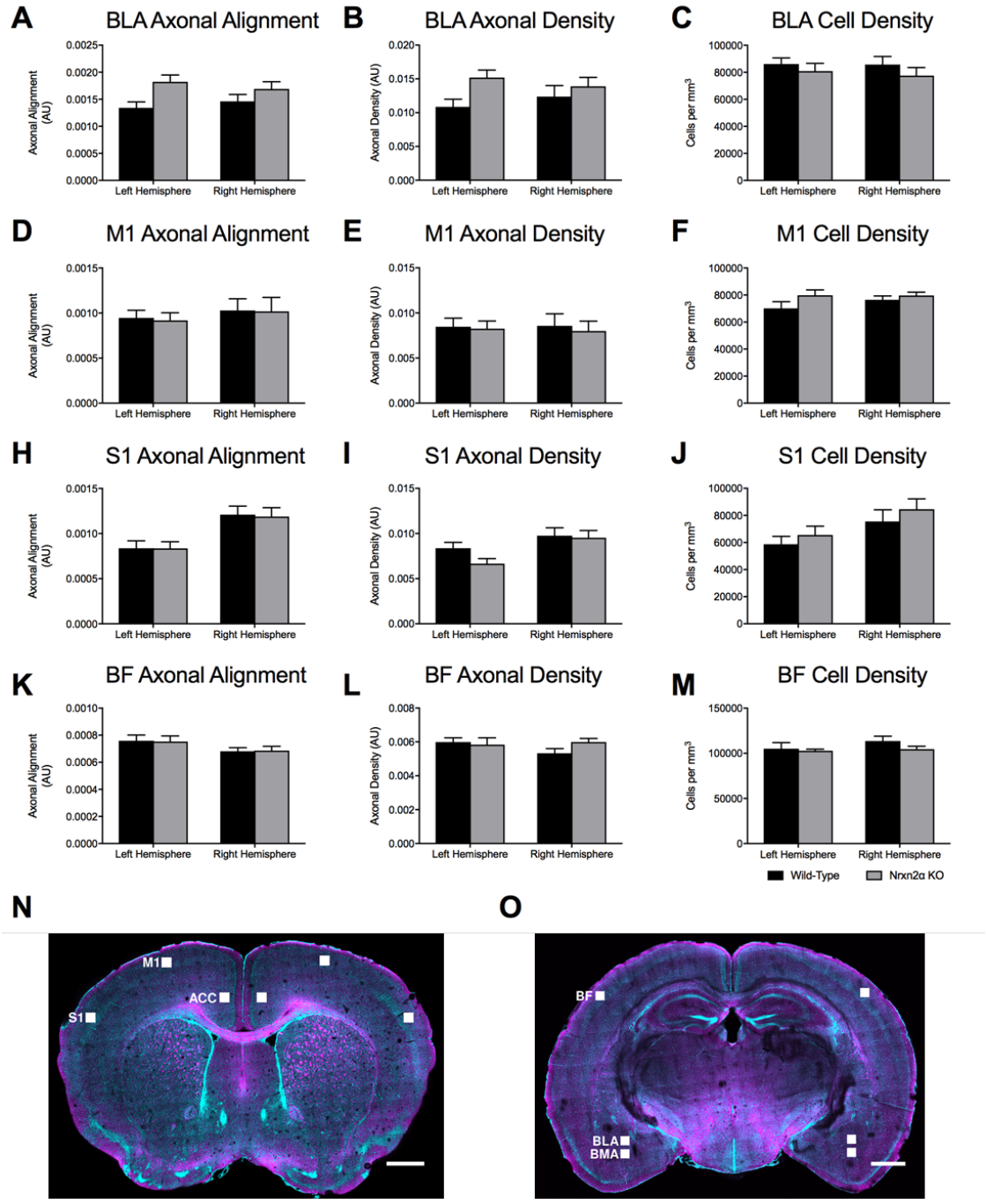

CLARITY-derived quantification of fibres and cell density within the basolateral amygdala (BLA) and control regions (**A**) Although there were trends towards increased axonal alignment and fibre density (**B**) in Nrxn2α KO mice, no significant differences were found. (**C**) Cell density in the BLA was similar between the genotypes. Statistical analysis (Supp. Table 4) was performed for the primary motor cortex (M1; **D-F**), primary somatosensory cortex (S1; **H-J**) and the barrel field (BF; **K-M**). No genotypic differences were found for any measure within these cortical regions. (N-O) CLARITY images of the scanned regions of interest. Error bars represent s.e.m. Wild-type n=6, Nrxn2α KO n=6.

References

1. Wu D, Xu J, McMahon MT, van Zijl PC, Mori S, Northington FJ, et al. In vivo high-resolution diffusion tensor imaging of the mouse brain. NeuroImage. 2013;83:18-26.
2. Vo A, Sako W, Dewey SL, Eidelberg D, Ulug AM. 18FDG-microPET and MR DTI findings in Tor1a+/- heterozygous knock-out mice. Neurobiology of disease. 2015;73:399-406.
3. Kumar M, Duda JT, Hwang WT, Kenworthy C, Ittyerah R, Pickup S, et al. High resolution magnetic resonance imaging for characterization of the neuroligin-3 knock-in mouse model associated with autism spectrum disorder. PloS one. 2014;9(10):e109872.
4. Ruest T, Holmes WM, Barrie JA, Griffiths IR, Anderson TJ, Dewar D, et al. High-resolution diffusion tensor imaging of fixed brain in a mouse model of Pelizaeus-Merzbacher disease: comparison with quantitative measures of white matter pathology. NMR in biomedicine. 2011;24(10):1369-79.
5. Kim S, Pickup S, Fairless AH, Ittyerah R, Dow HC, Abel T, et al. Association between sociability and diffusion tensor imaging in BALB/cJ mice. NMR in biomedicine. 2012;25(1):104-12.
6. Jones DK. The effect of gradient sampling schemes on measures derived from diffusion tensor MRI: a Monte Carlo study. Magnetic resonance in medicine. 2004;51(4):807-15.
7. Lebel C, Benner T, Beaulieu C. Six is enough? Comparison of diffusion parameters measured using six or more diffusion-encoding gradient directions with deterministic tractography. Magnetic resonance in medicine. 2012;68(2):474-83.
8. Ni H, Kavcic V, Zhu T, Ekholm S, Zhong J. Effects of number of diffusion gradient directions on derived diffusion tensor imaging indices in human brain. AJNR American journal of neuroradiology. 2006;27(8):1776-81.
9. Hasan KM, Parker DL, Alexander AL. Comparison of gradient encoding schemes for diffusion-tensor MRI. Journal of magnetic resonance imaging : JMRI. 2001;13(5):769-80.
10. Schindelin J, Arganda-Carreras I, Frise E, Kaynig V, Longair M, Pietzsch T, et al. Fiji: an open-source platform for biological-image analysis. Nature methods. 2012;9(7):676-82.
11. Peng H, Ruan Z, Long F, Simpson JH, Myers EW. V3D enables real-time 3D visualization and quantitative analysis of large-scale biological image data sets. Nature biotechnology. 2010;28(4):348-53.
12. Linkert M, Rueden CT, Allan C, Burel JM, Moore W, Patterson A, et al. Metadata matters: access to image data in the real world. The Journal of cell biology. 2010;189(5):777-82.
13. Perge JA, Niven JE, Mugnaini E, Balasubramanian V, Sterling P. Why do axons differ in caliber? The Journal of neuroscience : the official journal of the Society for Neuroscience. 2012;32(2):626-38.
14. Otsu N. A Threshold Selection Method from Gray-Level Histograms. IEEE Transactions on Systems, Man, and Cybernetics. 1979;9(1):62-6.
15. Rosin P. Unimodal thresholding. Pattern Recognition. 2001;34(11):2083-96.
16. Lee T, Kashyap R, Chu C. Building Skeleton Models via 3-D Medial Surface Axis Thinning Algorithms. CVGIP: Graphical Models and Image Processing. 1994;56(6):462-78.
17. Kerschnitzki M, Kollmannsberger P, Burghammer M, Duda GN, Weinkamer R, Wagermaier W, et al. Architecture of the osteocyte network correlates with bone material quality. Journal of bone and mineral research : the official journal of the American Society for Bone and Mineral Research. 2013;28(8):1837-45.
18. Franklin K, Paxinos G. The Mouse Brain in Stereotaxic Coordinates: Academic Press; 2008.

Figure 1

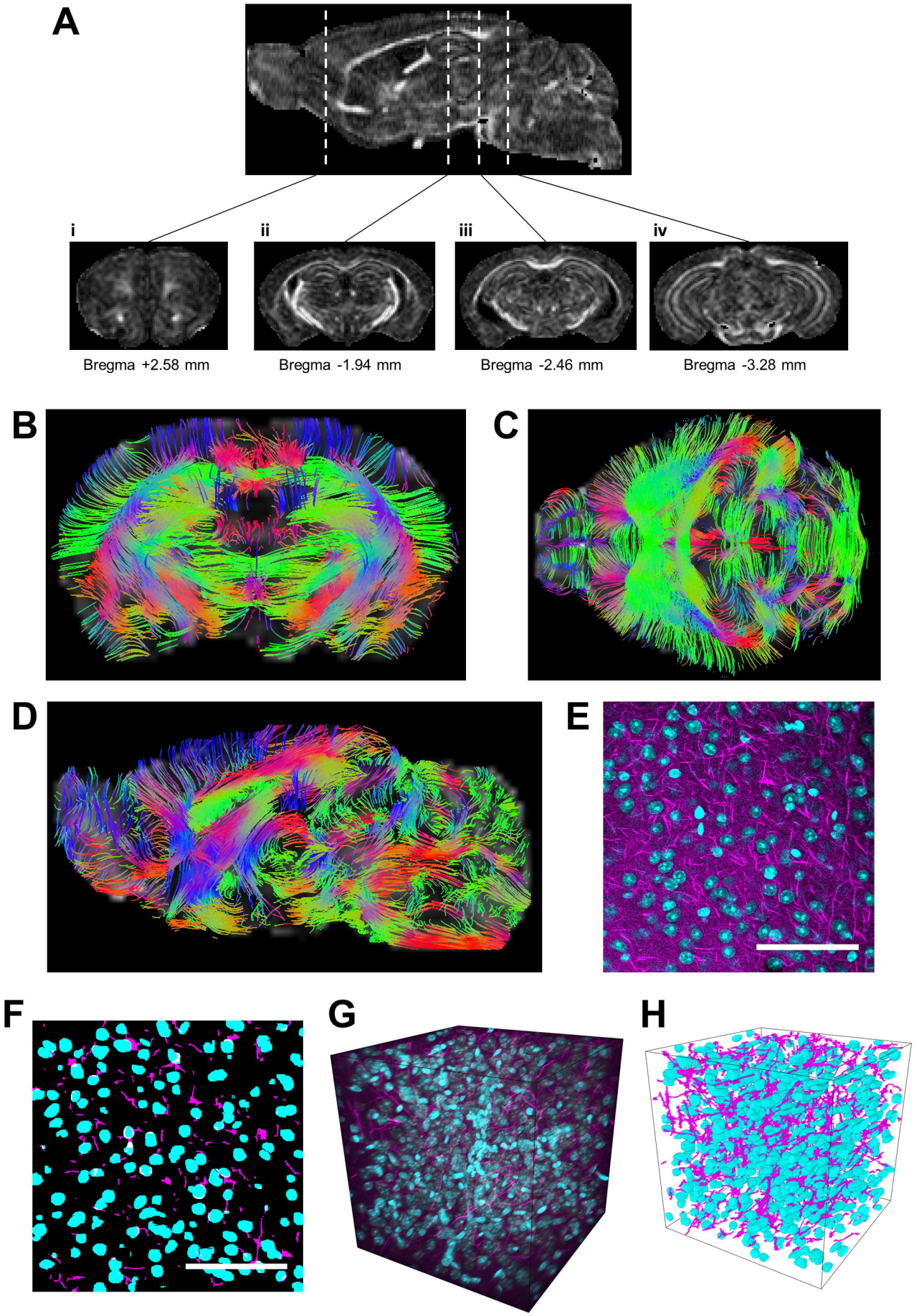
A
i
ii
iii
iv
Bregma +2.58 mm
Bregma -1.94 mm
Bregma -2.46 mm
Bregma -3.28 mm
B
C
D
E
F
G
H

Figure 2

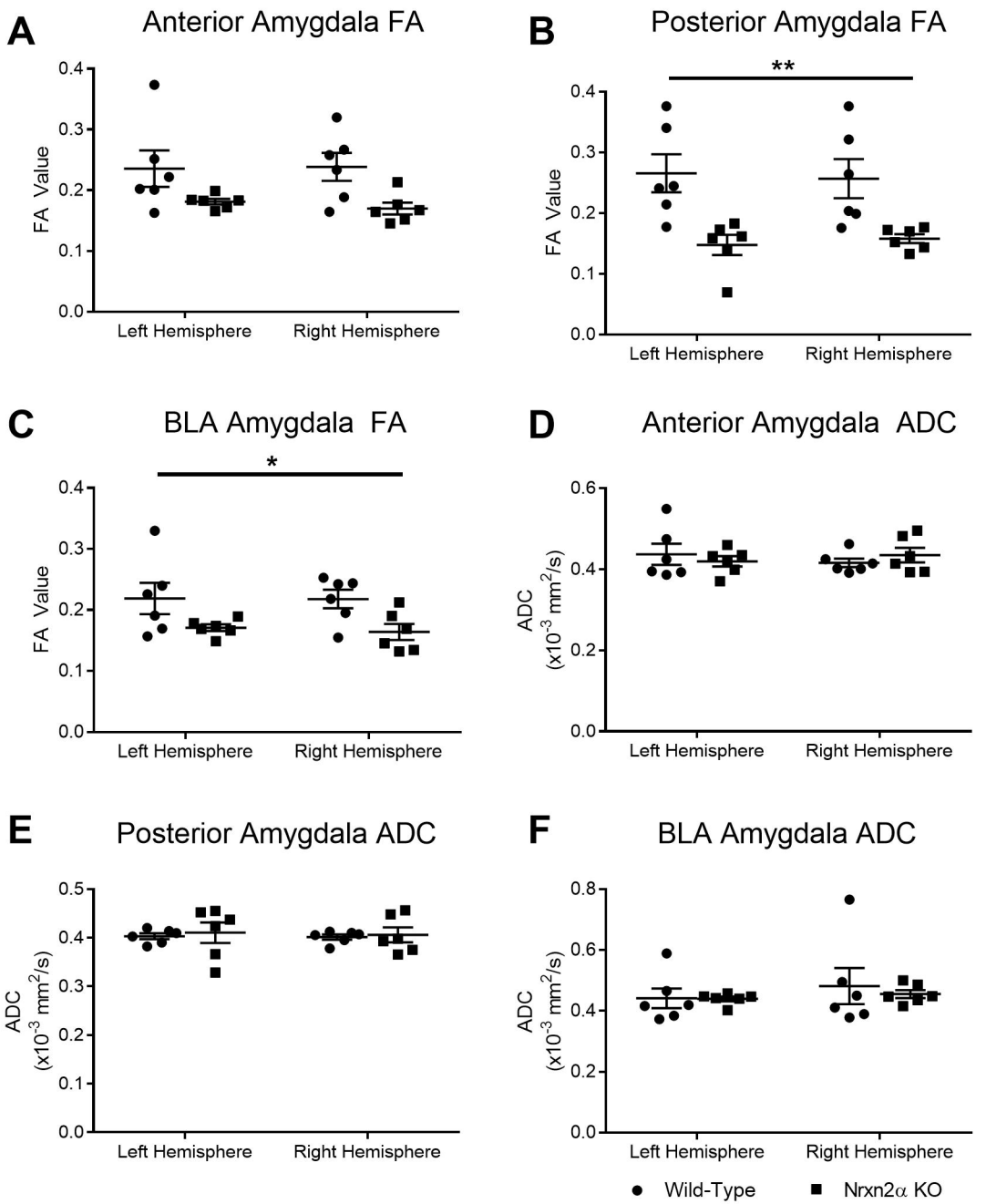
A
Anterior Amygdala FA
FA Value
0.4
0.3
0.2
0.1
0.0
Left Hemisphere
Right Hemisphere
B
Posterior Amygdala FA
**
FA Value
0.4
0.3
0.2
0.1
0.0
Left Hemisphere
Right Hemisphere
C
BLA Amygdala FA
*
FA Value
0.4
0.3
0.2
0.1
0.0
Left Hemisphere
Right Hemisphere
D
Anterior Amygdala ADC
ADC
(x10^{-3} mm^2/s)
0.6
0.4
0.2
0.0
Left Hemisphere
Right Hemisphere
E
Posterior Amygdala ADC
ADC
(x10^{-3} mm^2/s)
0.5
0.4
0.3
0.2
0.1
0.0
Left Hemisphere
Right Hemisphere
F
BLA Amygdala ADC
ADC
(x10^{-3} mm^2/s)
0.8
0.6
0.4
0.2
0.0
Left Hemisphere
Right Hemisphere
Wild-Type
Nrxn2α KO

Figure 3

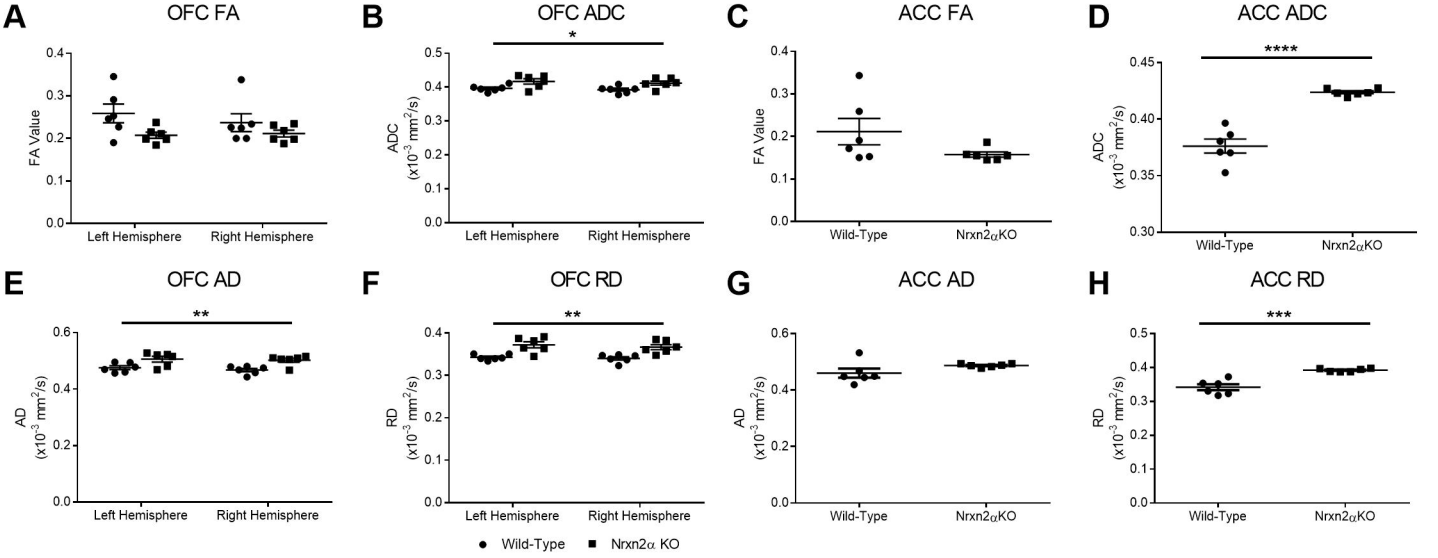
A
OFC FA
FA Value
0.0
0.1
0.2
0.3
0.4
Left Hemisphere
Right Hemisphere
B
OFC ADC
*
ADC
(x10^{-3} mm^2/s)
0.0
0.1
0.2
0.3
0.4
0.5
Left Hemisphere
Right Hemisphere
C
ACC FA
FA Value
0.0
0.1
0.2
0.3
0.4
Wild-Type
Nrxn2αKO
D
ACC ADC
****
ADC
(x10^{-3} mm^2/s)
0.30
0.35
0.40
0.45
Wild-Type
Nrxn2αKO
E
OFC AD
**
AD
(x10^{-3} mm^2/s)
0.0
0.2
0.4
0.6
Left Hemisphere
Right Hemisphere
F
OFC RD
**
RD
(x10^{-3} mm^2/s)
0.0
0.1
0.2
0.3
0.4
Left Hemisphere
Right Hemisphere
G
ACC AD
AD
(x10^{-3} mm^2/s)
0.0
0.2
0.4
0.6
Wild-Type
Nrxn2αKO
H
ACC RD
***
RD
(x10^{-3} mm^2/s)
0.0
0.1
0.2
0.3
0.4
0.5
Wild-Type
Nrxn2αKO
Wild-Type
Nrxn2α KO

Figure 4

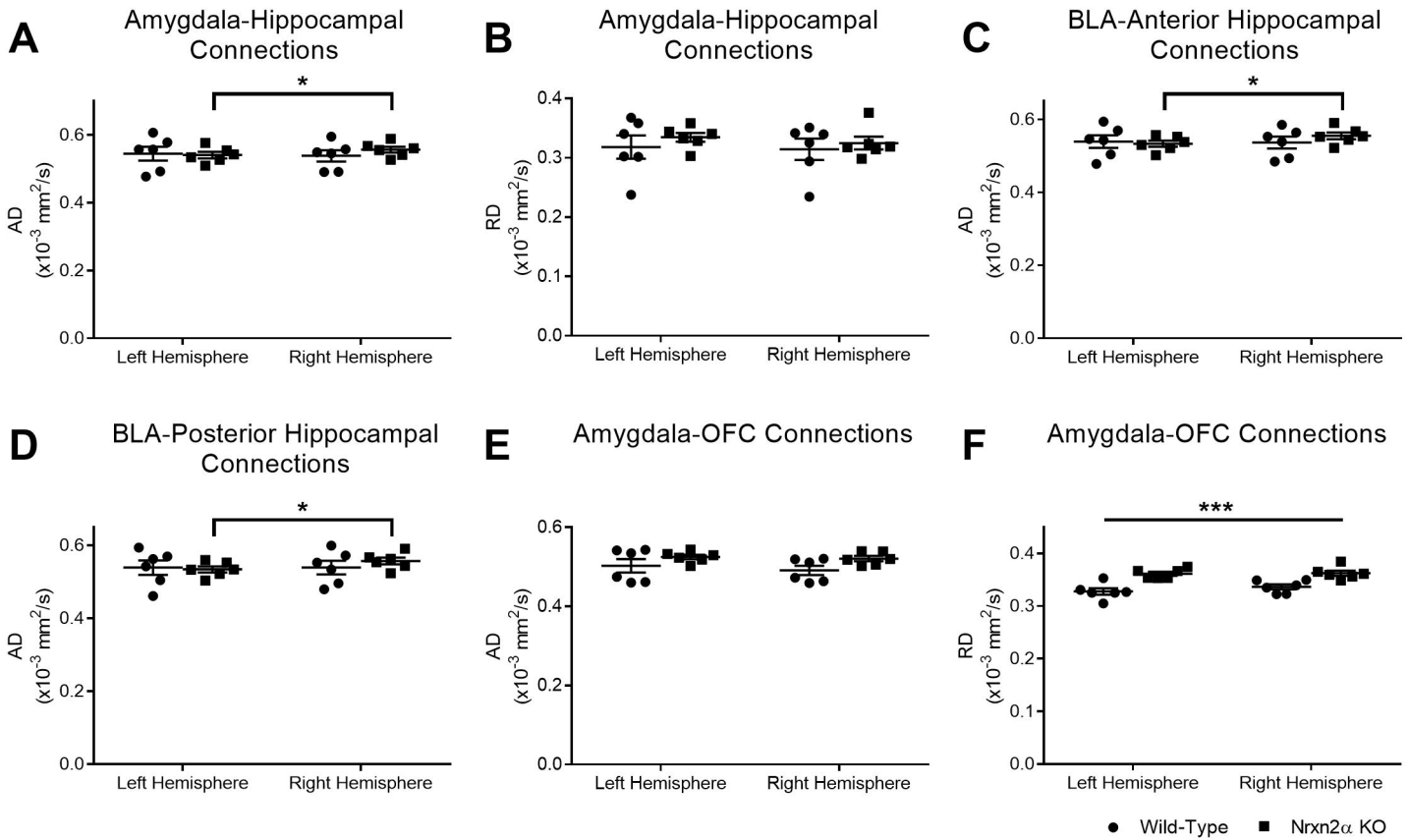
A
Amygdala-Hippocampal Connections
AD (x10^{-3} mm^2/s)
0.0
0.2
0.4
0.6
*
Left Hemisphere
Right Hemisphere
B
Amygdala-Hippocampal Connections
RD (x10^{-3} mm^2/s)
0.0
0.1
0.2
0.3
0.4
Left Hemisphere
Right Hemisphere
C
BLA-Anterior Hippocampal Connections
AD (x10^{-3} mm^2/s)
0.0
0.2
0.4
0.6
*
Left Hemisphere
Right Hemisphere
D
BLA-Posterior Hippocampal Connections
AD (x10^{-3} mm^2/s)
0.0
0.2
0.4
0.6
*
Left Hemisphere
Right Hemisphere
E
Amygdala-OFC Connections
AD (x10^{-3} mm^2/s)
0.0
0.2
0.4
0.6
Left Hemisphere
Right Hemisphere
F
Amygdala-OFC Connections
RD (x10^{-3} mm^2/s)
0.0
0.1
0.2
0.3
0.4
***
Left Hemisphere
Right Hemisphere
Wild-Type
Nrxn2α KO

Figure 5

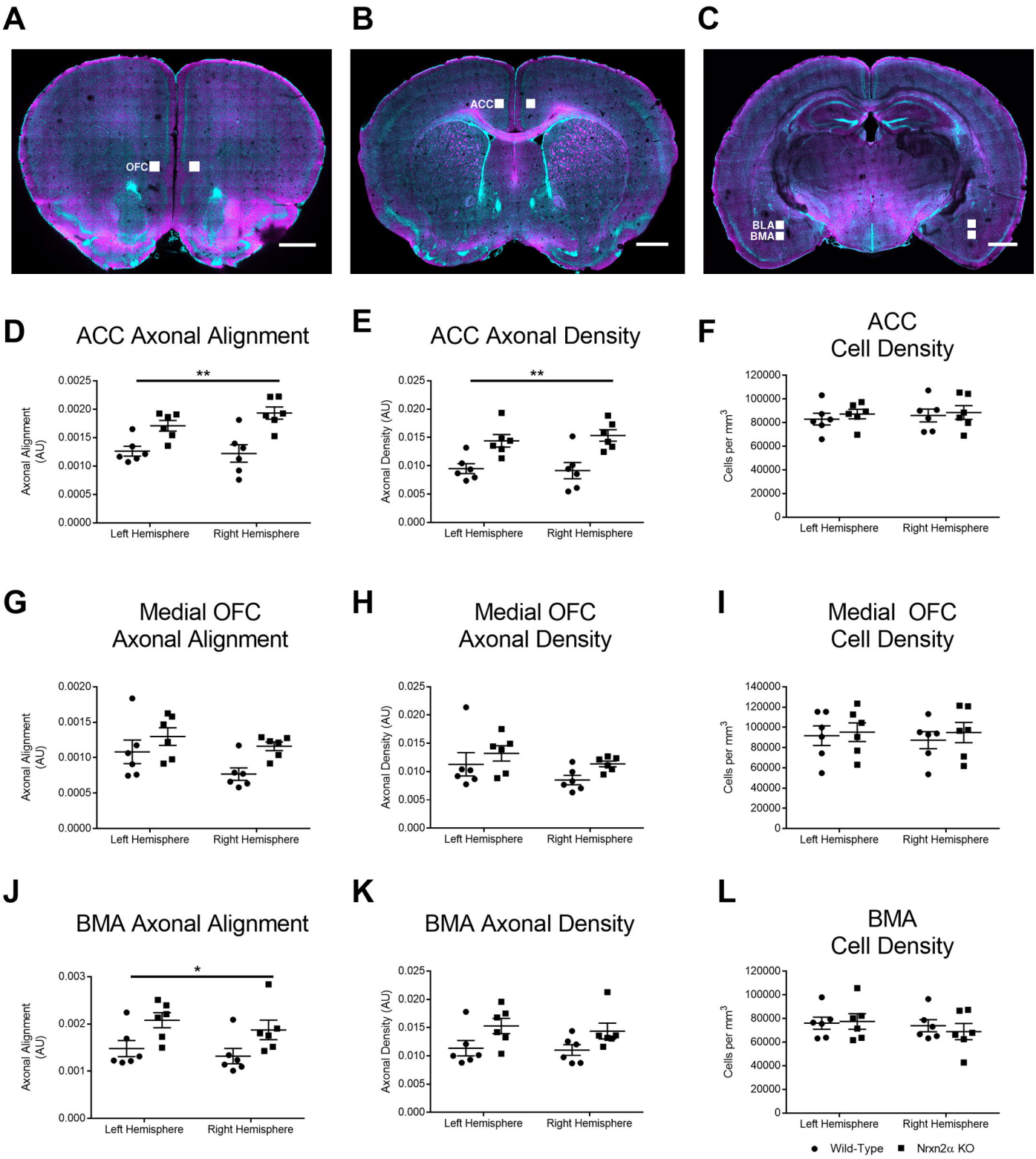
A
B
C
OFC
ACC
BLA
BMA
D
ACC Axonal Alignment
Axonal Alignment (AU)
**
Left Hemisphere
Right Hemisphere
E
ACC Axonal Density
Axonal Density (AU)
**
F
ACC Cell Density
Cells per mm3
G
Medial OFC Axonal Alignment
H
Medial OFC Axonal Density
I
Medial OFC Cell Density
J
BMA Axonal Alignment
*
K
BMA Axonal Density
L
BMA Cell Density
Wild-Type
Nrxn2α KO